Interzeolite Conversion and the Role of Aluminum: Toward Generic Principles of Acid Site Genesis and Distributions in ZSM-5 and SSZ-13

Julien Devos,† Sven Robijns,† Cédric Van Goethem,‡ Ibrahim Khalil,† and Michiel Dusselier*†

† Center for Sustainable Catalysis and Engineering (CSCE), KU Leuven, Celestijnenlaan 200F, B-3001 Leuven, Belgium.

‡Centre for Membrane Separations, Adsorption, Catalysis and Spectroscopy for Sustainable Solutions (cMACS), Celestijnenlaan 200F, B-3001 Leuven, Belgium.

Interzeolite transformation, Acid site distribution, Al distribution, Divalent cation exchange, Fourier transform infrared spectroscopy, MFI, ZSM-5, CHA, SSZ-13, Zeolite Synthesis

ABSTRACT:

The performance of zeolite catalysts not only depends on the strength and number of Brønsted acid (or exchange) sites but also on synergistic effects derived from their proximity in particular, and their distribution in general. Little is known on the genesis of acid sites and site distributions in hydrothermal zeolite synthesis. By an extensive study of five crystallization systems yielding ZSM-5 (MFI) and SSZ-13 (CHA), with a focus on interzeolite conversion (IZC) methods, several synthesis factors and mechanisms that are key in determining the output acid site distribution have been identified. Key in this study were temporal synthesis profiles while probing the distribution and evolution of proximal acid sites with divalent cation capacity measurements. Over the course of different crystallizations, changing local charge distributions are detected, notably within crystalline materials upon prolonged exposure (maturation). Aluminum is clearly the key driver in IZC syntheses, from a charge, dissolution, concentration and mobility point of view. Quasi generic principles for IZC syntheses are proposed, distinguishing between Al-loving and Al-averse systems, enabling a new degree of control over the acidity and ion-exchange properties of zeolites, of use to tailoring catalytic activity.

TOC

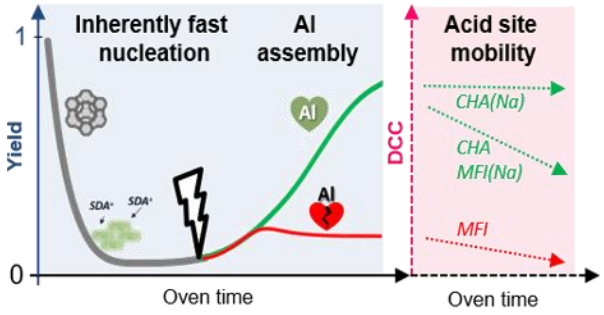
1
0
Yield
Inherently fast nucleation
Al assembly
Al
Al
SDA+
SDA+
Oven time
DCC
Acid site mobility
CHA(Na)
CHA
MFI(Na)
MFI
Oven time

1. Introduction

Zeolite catalysis is influenced by acid site proximity at the short-range order. Synergies of proximate acid sites have been proposed to influence activity in certain reaction pathways via improved sorption stability and/or transition-state stabilization, yielding more active and selective catalysts.[1–6] Despite the influence of external surfaces (small crystals), defect sites (from steaming), or amorphous fractions,[7] most acid sites in zeolites can be related to internal bridging Si_{IV}−OH−Al_{IV} hydroxyls in the framework. Therefore, the manipulation and understanding of (atomic range) Al distributions, and their genesis, is a crucial domain to further advance zeolite catalysts.

Most recent studies on short-range Al distributions have deduced 'thermodynamic' synthesis outcomes based on localized charge balances at the cage level between a positively charged (organic) structure-directing agent (O)SDA and the negatively charged framework from either aluminum or defect sites.[8–15] Furthermore, Al separation rules such as Löwenstein rule[16] or Dempsey's rule[17] and the intrinsic thermodynamic preference of Al for particular T-sites (framework dependent)[18] also seem to influence the short-range Al distribution in synthesized zeolites, despite the strong influence of kinetic processes during zeolite crystallization.[19,20] The use of alternative Si and Al sources −and other recipe alterations− may provoke Al distribution outcomes unexpected from a charge-balancing perspective.[5,21–24] A possible explanation for these outcomes can be related to the state of the heterogeneous precursor, unable to reorganize into neatly charge-balanced Al arrangements in time.[24] Hence, certain (kinetically fast) synthesis methods may be interesting to create zeolites with proximate Al having beneficial synergetic acid sites for particular catalytic applications.

A promising approach in this respect is zeolite synthesis via interzeolite conversion (IZC) resulting in fast and sometimes selective syntheses.[25–28] In IZC, an existing zeolite is used as Si and Al source to create a more valuable zeolite product. The success of IZC (and seeding) has been hypothetically assigned, for a long time, to *nanoparts* with structural similarities (e.g. 'common building units' between mother and product zeolite),[27–29] however, it has been recently questioned whether such structural features are really vital for interzeolite conversion or seeded growth.[30–34] For example, FAU-to-MOR IZC (with MFI as intermediate metastable phase) has been reported (without the use of OSDA).[32] None of these structures have common building blocks and the MFI-to-MOR transformation is one from a denser to a more open structure, which is unexpected from a thermodynamic perspective.[35,36] Clearly, a single descriptor is inadequate to explain the complex processes related to a successful IZC crystallization,[26,30] and recent studies have investigated different synthetic parameters that relate more closely to growth kinetics.[24,30] Perhaps, the proposed *nanoparts* may just serve as non-selective surfaces sparking heterogeneous nucleation.[37,38] A recent publication on AEI and AFX, starting from FAU, found matching lattice parameters −proportional to the Al content− as an important prerequisite for successful formation of these particular Al-containing frameworks.[39] This suggests heterogeneous nucleation starting at ordered FAU leftovers and highlights the key-role of Al and source dissolution. Moreover, investigations of interzeolite conversion to frameworks with intrinsic preference for high Al contents (e.g. CHA[18]) indicate the conservation of short-range Al distributions, as seen throughout FAU-to-CHA transformation.[40] A similar conclusion was drawn by our group for a high Si FAU-to-CHA IZC system (Devos *et al.*),[24] where we demonstrated that the very fast (<3h) procedure runs via an intermediate Al-rich phase prior to nucleation, as seen in a temporal analysis of liquid and solid fractions. The resulting crystalline Si-rich CHA (Si/Al up to 35) shows a remarkably

high content of acid site (Al) proximity as deduced from cobalt (divalent cation) titration. Most interestingly, the study also demonstrated the effect of prolonged hydrothermal treatment on apparently 100% crystalline SSZ-13 (CHA). With time, the divalent cation capacity (DCC) dropped from Co/Al=0.31 after 3 h to 0.16 after 16 days (or even to 0.07 when conducted at 180°C), indicating changes in the internal acid sites distribution over time in 'mature' zeolites. The DCC parameter is based on a common cobalt titration method used to investigate the role of site proximity in zeolites.[20,21,41–43] These acid sites may also include non-crystalline acid sites in proximity to classic acid sites (e.g. Si_{IV}−OH−Al_{IV}), as recently detected by analyzing divalent cation titrations coupled with ^{1}H MAS NMR.[41] Note that in some cases of (low temperature) zeolite catalysis both Brønsted-Lewis[44,45] or Brønsted-Brønsted[41,46] synergies can improve certain reaction pathways with such non-crystalline protons in proximity to other acid sites. Despite the complex nature of room temperature Co-exchange and the complex relation between proximate acid sites and zeolite catalysis, it is accepted that the DCC parameter can be an effective experimental tool to scan and quantify synthesis outcomes for their potential for zeolite catalysis. In particular, DCC is an efficient method to pinpoint the most suitable zeolite host materials for redox chemistry −requiring divalent cations− as recently shown in Fe-SSZ-13 (CHA) for methane partial oxidation[24] and in Cu-SSZ-13 for NH_3-based selective catalytic reduction.[47]

The high tendency to position Al in proximate configurations in CHA, when IZC is applied as synthesis strategy,[24,40,48] prompted an investigation of other common synthesis systems to corroborate the generic nature of IZC for high divalent cation capacity. Therefore −in this study− a controlled high silica (Si/Al = 40) FAU-to-MFI IZC system was investigated with and without sodium and compared with classic synthesis from amorphous sources as well as to the FAU-to-CHA IZC system. The chemical and structural properties (and their genesis) were followed during

each stage of the synthesis evolution and the divalent cation capacity of the resulting solids was investigated. The inherent advantages of IZC as strategy for synthesis systems fond of Al (such as in CHA crystallization) were distinguished, contrasting the slow MFI crystallization system using solely organic cations.

2. Experimental section:

2.1. Zeolite synthesis

2.1.1. Synthesis series. All synthesis series *([TPA;Na]^{IZC}*; *[TPA]^{IZC}*; *[TPA;Na]$^{Am.}$*; *[TPA]$^{Am.}$*, and *[TMAda]^{IZC}*) were made from stoichiometrically identical synthesis batches: SiO2: 0.025Al: 0.35 SDA^+: 0.35OH^-:12.5H_2O. The abbreviation between bracket represents the used structure directing agents (SDAs) in the synthesis mixture. TPA represents tetrapropylammonium (OH-form, 40 wt %, Sachem), a common organic SDA (OSDA) to synthesize ZSM-5 (MFI framework). TMAda abbreviates for trimethyladamantyammonium (OH-form, 20 wt %, Sachem), the OSDA for SSZ-13 synthesis (CHA). 'Na' represents sodium (OH-form, 20 wt %, from >98 wt % NaOH pellets, VWR). In some synthesis series, sodium was used together with the OSDA in equimolar content while the composition was maintained at a cationic charge density (($OSDA^+$ + Na^+)/Al= 14). The suffix 'IZC' is added if CBV780 (zeolyst) −a high Si-FAU (US-Y; Si/Al=40) zeolite− was used as Si and Al source.[25] The suffix 'Am.' was used for conventional gel synthesis starting from colloidal silica (LUDOX HS-40, Sigma Aldrich) and amorphous aluminum hydroxide (Sigma Aldrich).

2.1.2. Synthesis procedure. All syntheses were prepared with strict control over reactants and external conditions. The OSDA from the various synthesis systems, either TMAdaOH or TPA-OH were added to a Teflon liner together with deionized water (18.2 $M\Omega.cm^{-1}$) and eventual sodium. All solutions were homogenized by internal stirring (PTFE stirring bar, 20 x 6 mm) before introduction of the source materials. The Si-source was added prior to the Al source in the case of

'Am.' type syntheses. The complete mixtures were internally stirred until a homogenous mixture was obtained (~1 minutes for IZC syntheses, 5 minutes for Am* syntheses). Next, the Teflon liners were inserted in the corresponding stainless steel autoclaves and heated in a mechanical convection oven (Heratherm, ThermoSientific) under 600 rpm internal stirring (heat resistant multi-position stirring plate, 2mag) at the corresponding synthesis temperature. All hydrothermal treatments were performed at 160°C, unless specified otherwise. Syntheses were stopped after hydrothermal treatment, cooled and the solid phase was separated from its synthesis liquor by centrifugation (6000 rpm, ≥5 minutes, Thermo Fisher Scientific SL16). Both supernatant ('liquid' phase) and sediment ('solid' phase) were collected for further characterization (2.3). The solids were further washed (±50 mL solvent per g solids) with deionized water (18.2 $M\Omega.cm^{-1}$) until the supernatant showed pH values below 9 (at least 3 times). After a final washing step with acetone the solids were oven-dried overnight at 100°C, yielding the as-synthesized materials. The OSDA in the zeolite pores was removed by calcination in static air at 580°C for 6 h after ramping the furnace at 1°C/min from ambient conditions (LV9/11, Nabertherm).

Short-timed synthesis experiments (<3h) were actively cooled with a reproducible water batch cooling for 15 minutes to eliminate inter-sample variations related to the heat resistance of reactor systems. For the same reason, all very short-timed (≤1.25 h; sodium free) syntheses were executed exclusively in 23 ml Teflon cups in stainless steel autoclaves (Acid digestion vessel 4749, Parr instruments), while all sodium containing syntheses were executed in 25 ml PTFE cups in stainless steel autoclaves (Xian Toption Instrument Co.).

2.2. Divalent cation capacity (DCC) quantification

The divalent cation capacity (DCC) was determined by aqueous Co-exchange and ICP-AES, closely similar to the method of Dědeček *et al.*[21] under ambient conditions, to probe specific atomic

configurations (proximate Al). This method, adapted by multiple authors[49–52] studying Al distributions, used a 0.05M $Co(NO_3)_2$ solution, starting from sodium exchanged zeolites and identical to the DCC method applied earlier in ref.[24]

First, H^+-(or partial Na^+/H^+)-CHA or MFI were converted to the Na^+-form via aqueous phase ion-exchange using 150 ml of an aqueous 0.5 M NaCl (>99%, VWR) solution per g of solids at ambient conditions under stirring. After every exchange step, the samples were centrifugated and the liquid decanted. This procedure was repeated 3 times with respectively 16 h, 8 h, and 16 h of exchange times. After the final exchange the solids were separated by centrifugation and washed at least three times with deionized water (>150 ml per g solids, 18.2 MΩ). Subsequently, Na^+-form solids were oven-dried at 100°C. The Co exchange procedure was similar to Na exchange, using 150 ml of an aqueous 0.05 M $Co(NO_3)_2$ (>99%, Acros Organics) solution per g Na-exchanged zeolite at ambient conditions under stirring. This procedure was repeated 3 times with respectively 16 h, 8 h, and 16 h exchange times. After exchange the solids were separated by centrifugation and washed at least three times (>150 ml per g solids, 18.2 MΩ). (Co,Na)-form zeolites are oven-dried at 100°C overnight.

2.3. Characterization methods

X-ray powder diffraction. The structure and crystallinity of the zeolites were confirmed by X-ray powder diffraction (PXRD) on a high-throughput STOE STADI P Combi diffractometer in transmission mode with focusing Ge(111) monochromatic X-ray inlet beams (λ = 1.5406 Å, Cu Kα source). For each sample, a beam time of 10 minutes is used. Relative crystallinity was quantified on as-made MFI materials using the area under the peaks at 7.9°, 8.7° and in the range between 22.7 – 24.5° against a reference sample. For CHA materials, the selected peak areas were under 9.5°, 16.2° and 20.9°.

Nitrogen physisorption. Porosity is measured by nitrogen physisorption (Tristar II 3020, micrometrics) at -196°C on calcined and dried samples (6 h at 300°C). The relative nitrogen pressure was varied between 0.01 and 0.99 (p/p_0). The t-plot method (Harkins and Jura) on the adsorption branch is used to determine micropore volumes.

ICP-AES. The elemental analysis was performed using an inductively coupled plasma-atomic emission spectrometer (ICP-AES, Perkin Elmer Optima 3300 DV) with signal for Co, Fe, Al and Si at 308.2, 228.6, 238.2 and 251.6nm respectively. Before ICP-AES, the samples were dissolved using HF and aqua regia, neutralized using boric acid and diluted using 0.42 M HNO_3 in water.

Thermogravimetric analysis. TGA for as-synthesized SSZ-13 was performed on a TA Instruments TGA Q500. The relative content of occluded $TMAda^+$ and TPA^+ was measured between as weight loss between 200°C and 700°C using O_2 flow.

Transmission Electron Microscopy. TEM-samples were prepared by drop-casting a dispersion of the particles on a holey carbon-coated TEM grid (Cu, 300 mesh, Pacific Grid Tech Ltd.). TEM was performed using a JEOL ARM200F microscope operated at 200kV and equipped with a cold FEG and a probe aberration corrector. EDX analysis of the samples was performed using a Centurio EDX detector with a large solid angle of 0.98 steradians from a 100mm² detection area.

Fourier transform infrared spectroscopy. The nature and amount of the superficial sites (Bronsted acid sites, Lewis acid sites, and silanol groups) were determined by Fourier-transform infrared spectroscopy (FT-IR) using a Nicolet 6700 Spectrometer equipped with a deuterated triglycine sulfate (DTGS) detector. Prior to analysis, samples were pressed (10^7 Pa) into precisely weighted self-supported wafers of 5-10 mg/cm^2 and degassed *in-situ* at 400°C (5°C/min heating rate) for 1 h under vacuum (< 1mbar). After degassing, the cell was cooled to 150°C and a reference spectrum of the material was recorded with an accumulation of 64 scans at a resolution of 2 cm^{-1}.

All spectra were compared after a normalization to a constant disc mass (~8 mg/cm^2 of dry catalyst).

The quantification of the total amount of silanols of the zeolite samples was done by tracking the combination band (ν+δ)OH at around 4500-4600 cm^{-1} after degassing. This stretch, referring to silanol groups, was used instead of the fundamental ν(OH) at ~3740 cm$^{-1,}$ due to high dependence of the molar absorption coefficient of this latter "ε(ν_{Si-OH})" on the H-bonding interactions.[53,54] By contrast, it is possible to accurately calculate the amount of silanol groups using the (ν+δ)OH combination band with the respective "$\varepsilon_{(\nu+\delta)OH}$" determined by Gallas *et al.*, $\varepsilon_{(\nu+\delta)OH}$ = 0.16 cm/μmol.[55]

Pyridine adsorption and desorption was used for the quantification of Brønsted and Lewis acid sites. Thus, after degassing, the samples were exposed to 25mbar pyridine until saturation at 50°C. Thermal desorption was carried out for 20 minutes at 150°C under vacuum (< 1 mbar) in order to remove the physical adsorbed pyridine species. After each desorption step, a spectrum was recorded at 150°C and compared to the reference spectrum in order to identify the pyridine adsorbed species. The amount of Brønsted and Lewis acid sites were determined by integrating the area of the characteristic bands of pyridinium ions (PyH^+) "v8a" at ~1545 cm^{-1} and the coordinated pyridine species (PyL) "v19b" at ~ 1445 cm^{-1}, and using their corresponding molar absorption coefficient: ε(PyH^+) = 1.67 cm/μmol and ε(PyL) = 2.22 cm/μmol, respectively.[56]

3. Experimental Results:

3.1. Mechanistic investigation of IZC as crystallization system

The evolution of a controlled interzeolite transformation (FAU-to-MFI IZC; Si/Al=40) is investigated to gain insight into the factors governing acid site genesis, their location and the role of synthesis therein. Here, synthesis systems with identical molar composition and temperature

(160°C), described in section 3.1.1, are compared to equivalent crystallization systems without Na^+ (section 3.1.2). Later, in section 3.1.3, the crystallization behavior is compared to equivalent synthesis systems generating SSZ-13 (CHA) in order to generate detailed and more generic insights into IZC.

3.1.1. IZC towards ZSM-5 (MFI) using Na^+: [TPA;Na]^{IZC}

Siliceous FAU (US-Y; Si/Al=40) together with equimolar TPA and NaOH solutions are prepared (*[TPA;Na]^{IZC}*) in stoichiometrically identical compositions ($1SiO_2$: $0.025Al$: $0.175Na^+$: $0.175TPA^+$: $0.35OH^-$:$12.5H_2O$). In total 12 synthesis mixtures are hydrothermally treated at 160°C between 1 h and 12 days allowing a temporal study of the crystallization. In each synthesis system, the following synthesis stages are discerned in a similar fashion as in our earlier IZC work[24] : (I) incongruent source dissolution, (II) an equilibrium or induction phase with steady compositions, (III) crystallization towards a crystalline material, and finally, (IV) maturation of fully crystalline materials.

The synthesis of ZSM-5 (MFI) occurs so fast that the solids already demonstrate reflections in P-XRD after 1 h of oven time (Figure S1). Detailed evolution of the synthesis stages is summarized in Figure S2 containing the chemical compositions (Si/Al_S) and solid yields in time (1 h - 12 days). Nucleation and assembly (Stage III - Figure S2) occur so fast that the dissolution and equilibrium stages are not captured (Stages I-II in Figure S2). Around 40% crystallinity is observed after 1.5 h and full crystallinity is reached within 2 h (Figure S1). This is much faster than comparable synthesis systems based on amorphous sources (*[TPA;Na]$^{Am.}$*) that require more than 4 h prior to the first MFI trace observation (Section S.1.). As such, the assembly Stage (III) takes place in a short time, leading to fully crystalline ZSM-5 at 2 h or longer. The dry solid yield increases from 27 % after 1 h to 60% after 2 h and does not increase significantly with prolonged hydrothermal

treatment. Furthermore, the Si/Al ratio of the solids remains very stable in time at around 35, suggesting that no significant elemental changes are occurring on 'mature' zeolites after 2 h of crystallization (Stage IV - Figure S2). In addition, relatively homogeneous Al distributions are observed through crystalline *[TPA;Na]*^{IZC} solids as suggested by elemental mappings from TEM-EDX (Figure S3).

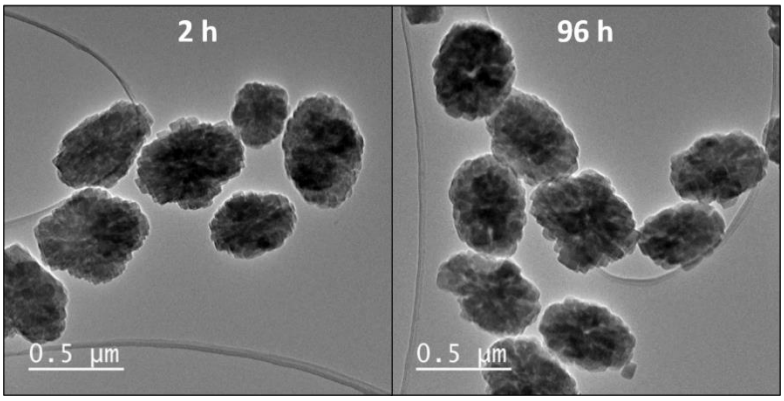

Figure 1. TEM images of solids with variable synthesis times (*[TPA;Na]*^{IZC}).

Structural characterizations methods (TEM and N_2 physisorption) did not reveal any significant differences in properties between fully grown calcined ZSM-5 samples after short crystallization (*2 h)* and after longer maturation times (*96h)* (Figure S4 and Table 1). Ellipsoid ZSM-5 aggregates, approximately 500 nm, are found (Figure 1). A further magnification highlights structured zones in rectangular protrusions with individual crystals sized 40-50nm (Figure S5). The small crystallites are aligned, indicating oriented attachment.[57] The characteristic morphology and dimension of these described ZSM-5 crystals are very similar as in so called 'finned' zeolites, which demonstrates superior catalyst performance due to improved mass transport.[58] Such type materials are achieved here via IZC without the requirement of using seeds. The image of finned (aggregated and oriented) crystals is confirmed by N_2 physisorption results (Figure S4) on calcined *[TPA;Na]*^{IZC} samples comparable to literature.[58] Typical micropore volumes for ZSM-5 (0.15 cm^3/g) and similar total pore volumes (0.25cm^3/g) are found after both 2 h and 4 days of

hydrothermal treatment (Figure S4). The observed mesoporosity can be linked to the interstitial volumes created by the nanocrystal aggregation, which is consistent with the detailed TEM view given in Figure S5. In a further section of this work (3.2.2) we demonstrate changing acid site distributions of these mature zeolites with synthesis time, hence, holding further implications for (tailoring) zeolite catalysis.

Pyridine FT-IR data indicate a nearly similar BAS/Al (~0.57) but changing LAS/Al content in the H-form samples of syntheses with oven times of 2 h and 4 days, respectively (Table 1). The LAS values are relatively high compared to larger industrial ZSM-5 samples, but in agreement with results for other fast crystallizing systems resulting in sub-micron crystals.[59,60]

Table 1. Amount of silanol groups and acid sites (pyridine adsorption/desorption 150°C) determined by FT-IR spectroscopy on the ZSM-5 samples originating from *[TPA;Na]^{IZC}* synthesis systems. The elemental data (bulk) originates from ICP-AES of the specific sample.

Sample	Si/Al	Co/Al	Al (µmol/g zeolite)	Co	BAS (µmol/g zeolite)	LAS	Si-OH	BAS/Al	LAS/Al	2 Co/BAS	2* Co/LAS
[TPA;Na]^{IZC}-2h	36	0.21	452	97	267	45	833	0.59	0.10	0.72	4.27
[TPA;Na]^{IZC}-96h	35	0.11	462	49	257	28	1035	0.56	0.06	0.38	3.52

Next to the detected shift in LAS contribution from FT-IR, some changes in time are detected by differential thermogravimetric data (DTG) on the as-synthesized ZSM-5 materials (Figure 2). Usually, ZSM-5 materials with Si/Al around 35 have a high weight loss peak at around 450°C assigned to TPA^+ in strong interaction with framework anionic charge (mostly due to $[AlO_{4/2}]^-$) and a small shoulder around 400°C caused by breakdown of less entangled (free) TPA^+ within the framework.[61–63] The latter peak may thus represent TPA^+ stabilized by (distant) silanol defects[64,65] or octahedral Al.[62] It also known that an increase of decomposition temperature of TPA^+ can be explained by stronger stabilization of TPA^+ in crystalline ZSM-5.[61–63] From Figure 2 (solid lines) we find more narrow and higher temperature DTG signals in samples with increasing synthesis times. Indeed, DTG profiles of partially crystalline *[TPA;Na]^{IZC}* samples at 1.5 h have a more

pronounced shoulder (400°C) than the fully crystalline samples (≥2 h). In addition, this shoulder is virtually absent after prolonged synthesis exposure (96 h). This disappearance points to subtle changes in internal stabilization between the present cations (TPA^+ and Na^+) and the anionic lattice density in fully crystalline ZSM-5 (*[TPA;Na]*^{IZC}) series.

As the directing cations (TPA^+ and Na^+) and source materials (Si and Al oxides) are the main players in this game of stabilization energies, variations thereof, i.e. *([TPA]*^{IZC}; *[TPA]*$^{Am.}$), were investigated in analogy with *[TPA;Na]*^{IZC} (section 3.1.2).

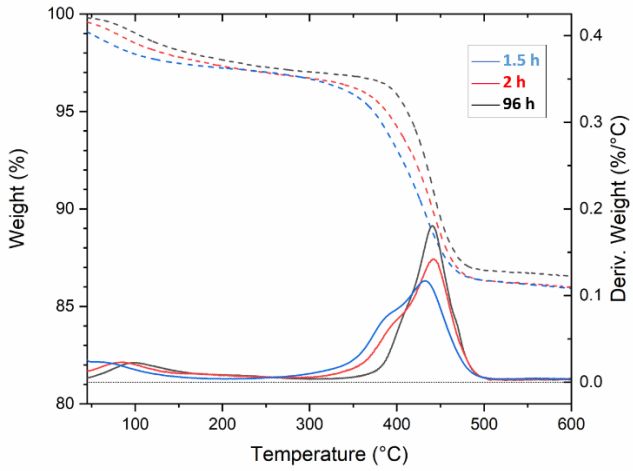

Figure 2. TGA (dotted lines) and DTG (solid lines) profiles at alternating synthesis durations *[TPA;Na]*^{IZC} indicating two different TPA interaction types. The relative crystallinity values of the materials are 40%, 84% and 68% after respectively 1.5 h, 2 h and 96 h in comparison to a 6 h reference.

3.1.2. IZC towards ZSM-5 (MFI) without Na^+: $[TPA]^{IZC}$.

Syntheses in the $[TPA]^{IZC}$ series are stoichiometrically identical to those from $[TPA;Na]^{IZC}$, however, they use double the amount of TPA^+ to exclude inorganic (alkali) cations ($1SiO_2$: $0.025Al$: $0.35TPA^+$: $0.35OH^-$:$12.5H_2O$) and thus avoid their effect on zeolite dissolution and structure direction.[66] In total, 45 synthesis mixtures were hydrothermally treated at 160°C, for times varying between 1 h and 12 days. The evolution of chemical compositions and crystallinity

of the solid products are summarized in Figure 3, with the three first stages of IZC (within 3 h) discerned in Figure 3A.

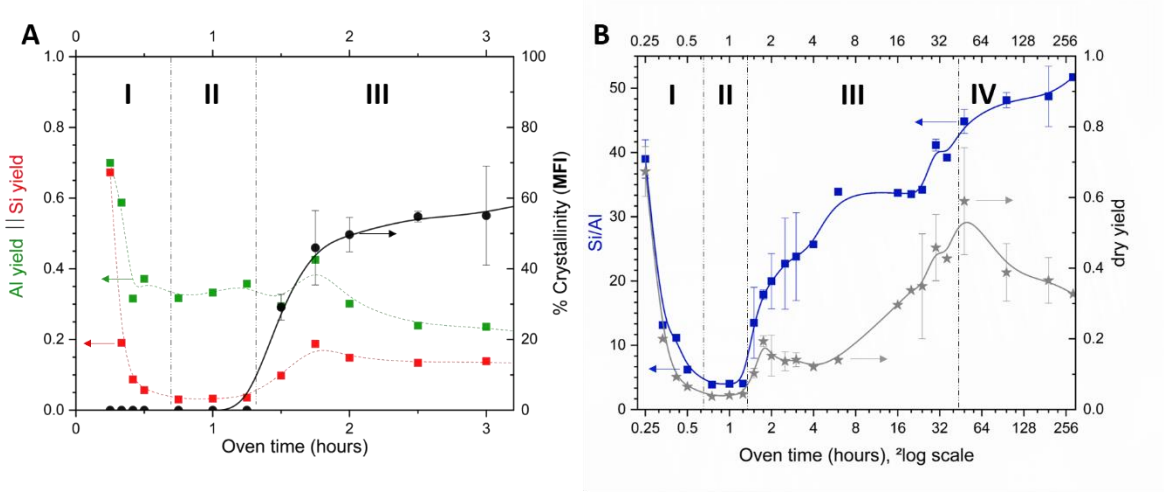

Figure 3. Properties of separated solids in *[TPA]*^{IZC} synthesis systems (high Si FAU-to-MFI IZC): **A)** Si and Al yield and MFI crystallinity during the initial stages of crystallization, **B)** Si/Al (blue) and dry yield (gray) of solid phases versus oven time (log scale) over 12 days. Error bars represent one standard deviation over synthesis replicates. The different temporal stages of IZC are shown (incongruent dissolution (I), induction (II), initial crystallization (III), and maturation (IV)).

IZC starts with (partial) dissolution of the FAU phase (Stage I) with heating. A strong decrease in the dry yield is observed between 15 and 20 minutes of oven time, as well as a significant pH drop from 13.9 to 12.5 (OH^- consumption) resulting in the loss of most long-range order as observed from powder X-ray diffraction (Figure S6A). This contrasts with room temperature aging, where less extended dissolution of the FAU sources is detected in time from P-XRD (Figure S7) and the lack of drop in pH with prolonged aging (pH stable at 13.9). During oven-heating, Si is dissolved much easier than Al, as apparent from the evolution of Si and Al yields recovered in the solid phase (Figure 3A - Stage I). Incongruent FAU dissolution is quite a generic phenomenon also observed in an identical set-up using TMAda as OSDA instead of TPA[24] or after post-synthetic treatments like desilication of high silica zeolites using organic amines.[67] Dissolution (Figure 3A - Stage I) seemingly ends within 45 minutes, when only a small fraction of total T-

atoms, i.e. 4% are contained in the Al-rich solids ($Si/Al_S = 4$) while the Si-rich supernatant solution ($Si/Al_L = \sim 80$) contains 96% of Si and 65% of the initial Al (from the FAU parent) at a pH of 12.5. With prolonged oven times (45 to 75 minutes), a clear distinct 'induction period' (Stage II) is depicted with little change in elemental composition of both the Al-rich solid phase and the Si rich liquids. Nonetheless, a diminishing fraction of FAU traces are still detected at 6.2° by P-XRD, even at the end of Stage II (Figure S6A - 75'). This illustrates that local T-atoms bonding may still change internally independently from the seemingly stable *'equilibrium phase'* (Stage II), as measured from ICP on the separable fractions (centrifugation).

The growth stage (Stage III) starts with the (fast) formation of nuclei before 1.5 h. At this time, the first MFI reflections are observed (Figure S6B), while any long-range order for FAU completely disappears. Within a short timeframe the yield sharply increases from 0.10 at 1.5 h up to a maximum of 0.19 at 1.75 h (Figure 3B). MFI crystallinity increases to around 45% after 1.75 h as compared to a fully crystalline sample (48 h synthesis). During this timeframe, the Al content remains relatively steady (Al-yield= ~0.35; Figure 3A), thus the initial increase in the yield after nucleation is the take-up of mostly Si, as witnessed by increasing Si/Al values in time (Figure 3B). The solid yield starts to drop between 1.75 h and 6 h from 0.19 to 0.12, respectively. On the other hand, the Si/Al_S ratio increase from 18 to 34 during this timeframe, meaning that the Al content of the solids is drastically reduced, as partially visualized in Figure 3A. With prolonged synthesis of $[TPA]^{IZC}$ (≥6 h), it can be observed that the dry yield slowly increases with time towards 50-60% after 48 h (Figure 3B). The end of the remarkably long crystallization stage (Stage III, 1.5h-48h) is marked by the highest crystallinities (Figure S6B) and a significant increase of the liquid pH from 12.5 to 13.4, as observed in other IZC systems.[68] This pH increase is most likely responsible

for the yield drop observed in the maturation stage (Stage IV ≥ 48 h). Fully crystalline materials are only found after 48 h (Stage IV - Figure 3B).

[TPA]^{IZC} thus exhibits a remarkable progression for Al and an unusual crystallization path. Despite the fast nucleation within 1.5 h, *[TPA]*^{IZC} demonstrates an unusually slow assembly phase (Stage III, 1.5 h-48 h) which contrasts to typically observed sigmoidal-shaped yield and crystallinity curves during the assembly Stage (III)[69]. The latter is also observed in *[TPA]*$^{Am.}$, starting from identical molar conditions, but using amorphous sources instead of FAU where complete crystallization is reached in only 19 h (Figure S10-S11). The slower assembly in *[TPA]*^{IZC} (48 h in total) contrasts the general (more or less accepted) assumption that IZC crystallizing systems are fast crystallizing systems (vide supra).[26,27] For *[TPA]*$^{Am.}$, as in most conventional systems, the period prior to nucleation is much longer than the actual assembly phase and the first X-ray long range order is only observed after 16 h of hydrothermal treatment (Figure S10). At this timeframe, the mixture is an amorphous gel (Si/Al = 25) which can serve as basis for solid-solid reorganizations into crystalline materials,[64] clearly contrasting the nucleation conditions during IZC. Elaborated details on conventional ZSM-5 (Si/Al = 40) synthesis performed in sodium-free standard conditions (*[TPA]*$^{Am.}$) can be found in the Supporting Information (Section S1).

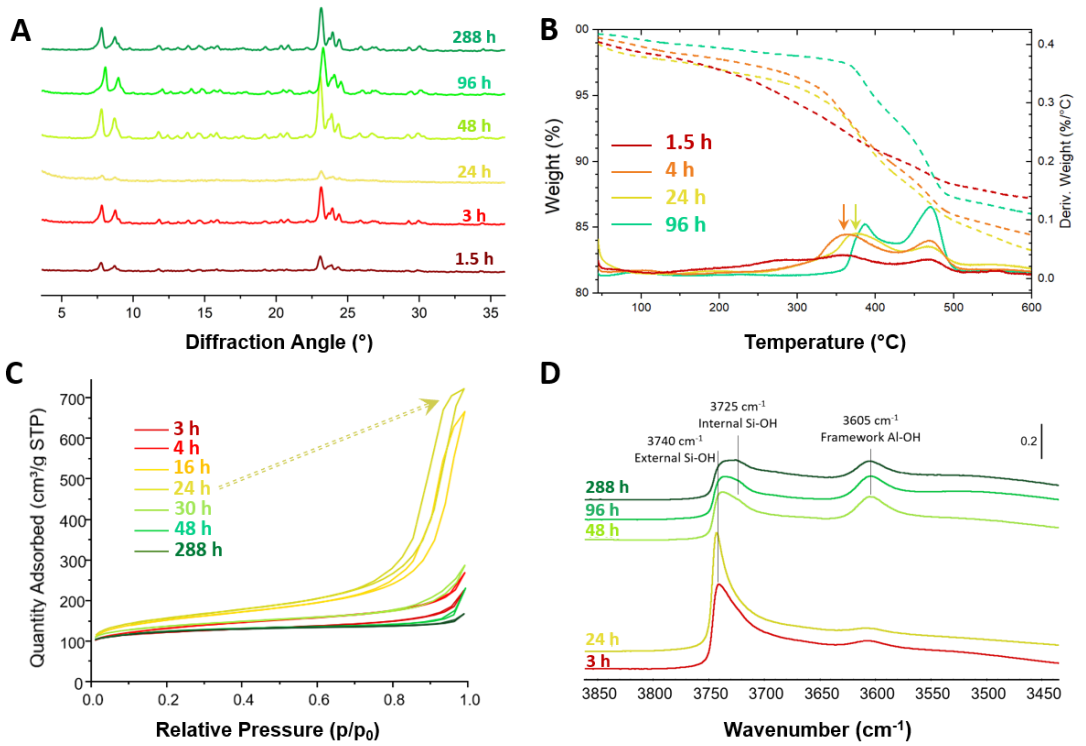

Figure 4. Comparison of solids at different oven times in *[TPA]*^{IZC} system: **A)** P-XRD of as-made solids, **B)** TGA (dotted lines) of as-made samples and corresponding DTG profiles (solid lines), **C)** N_2 sorption isotherms of calcined materials, **D)** FT-IR spectra in the OH stretching vibrations region.

Figure 4 gathers time-resolved results of four characterization methods (P-XRD, TGA, N_2 sorption, and FT-IR spectroscopy). Each of these witnesses the remarkable synthesis course in the crystallization stage (III) of *[TPA]*^{IZC} systems. During this long assembly stage (1.5 h -48 h), P-XRD demonstrates intermediate phases with lower crystallinity. The crystallinity of materials drops from ~60% at 3 hours to around 22% after 24 hours in comparison to a fully crystalline reference at 48 h (Figure 4A). The sudden crystallinity drop is explained by a strong increase in solid yield (Figure 3B) combined with the observation of amorphous materials from other techniques (see below). TGA of the first stages after nucleation reveals broad weight loss regions (200-500°C) for the as-made materials (Figure 4B, 1.5 h). The DTG peaks are shifting towards higher temperatures and become thinner in the first hours after nucleation (1.5 h - 4 h), which

corroborates with the initial crystallinity increases. DTG peaks remain in regions below 400°C during Stage III (also at 24 h), indicating TPA^+ charge-compensated by amorphous fractions, silanol defects or non-framework Al.[61,63] The DTG peaks around 465°C, characteristic of TPA^+ strongly interacting with framework anionic charge, only becomes dominant after complete crystallization (Stage IV; ≥48 h, e.g. 96 h in Fig. 4B). Meanwhile, a DTG peak centered between 350 and 400°C remains in place. Similar behavior was also evidenced from FT-IR spectroscopy.

The OH region of FT-IR (Figure 4D) of dry calcined Stage III samples shows a very faint signal for framework Al-OH stretching bonds (3605cm^{-1}) at 3 h, which even appears to be decreasing at 24 h. Despite all the samples having similar and high microporosities (micropore volume = 0.14 cm^3/g, Figure 4C), very few strong BAS (related to framework Al) can be quantified with adsorbed pyridine, especially compared to time-equivalent $[TPA;Na]^{IZC}$ samples (Table 1). Samples with 3 h and 24 h oven time show respectively 0.17 and 0.29 BAS per bulk Al (Table 2), as quantified from the band at 1545cm^{-1}. Solids at the end of Stage III (100% crystallinity, 48 h) show much higher BAS density (BAS/Al ≥ 0.48). We should note that the increase in BAS between 3 h and 24 h is associated with the increase of the Si-OH species, which can partially act as strong acidic silanol species in the amorphous phase (Figure 4D).[70,71] The increase in Si/Al ratio during Stage III, together with the DTG and FT-IR data suggest a very low tendency to assemble Al in framework positions when TPA^+ is used as the sole OSDA, contrasting to its fast-crystallizing counterpart with sodium ($[TPA;Na]^{IZC}$, section 3.1.1., Table 1).

Table 2. Amount and nature of acid sites for MFI originating from a *[TPA]^{IZC}* system as determined by pyridine adsorption/desorption at 150°C followed by FT-IR spectroscopy. The elemental data (bulk) originates from ICP-AES of the specific sample.

Sample	Si/Al	Co/Al	Al (µmol/g zeolite)	Co	BAS (µmol/g zeolite)	LAS	Si-OH	BAS/Al	LAS/Al	(BAS+LAS)/Al	2*Co/BAS
[TPA]^{IZC}-3h	31.6	0.10	509	50	86	56	1085	0.17	0.11	0.28	1.17
[TPA]^{IZC}-24h	34.0	0.27	472	129	137	118	1946	0.29	0.25	0.54	1.88
[TPA]^{IZC}-48h	43.5	0.08	373	30	206	49	712	0.55	0.13	0.68	0.29
[TPA]^{IZC}-96h	39.4	0.04	412	15	196	38	775	0.48	0.09	0.57	0.15
[TPA]^{IZC}-288h	51.7	0.03	316	11	202	41	1089	0.64	0.13	0.77	0.11

Transmission electron microscopy (TEM) of the solid phases demonstrates heterogeneously evolving solids during the assembly stage (Stage III). After 3 h of oven time, both large (>500nm) and cloudy 'ellipsoidal' particles sized ~300 nm are detected (Figure 5A). The larger particles show crystal habit typical for US-Y (FAU) particles,[39,72] despite the complete loss of long range order. In contrast to those, the ellipsoidal particles observed at 3 h are persistent in all solid stages. They are the sole particles obtained in 100% crystalline ZSM-5 at extended synthesis times (288 h; Figure 5C). Hence, the ellipsoidal particles after 3 h are presumed to be ZSM-5 crystals. These particles do not demonstrate significant changes in size or shape, but significantly differ in surrounding matter. The cloudiness of the ellipsoidal particles after 3 h is likely related to particle attachment via non-classical pathways[73–75] and contrasts to the more sharply-bordered FAU remnant particles.

TEM imaging of the 24 h sample (Figure 5B) demonstrates ZSM-5 crystals surrounded by large portions of irregularly shaped aggregates sized between 5 and 10 nm. Earlier, increasing yields and dropping crystallinities (Figure 4B) were found in samples in this time range, as such, the imaged irregular shaped aggregates are presumed to be amorphous. The latter corroborates with the FT-IR data extracted from the OH wavenumber region (Figure 4D). A very high content of external silanols (3740 cm^{-1}) and very few framework Al-OH bonds (3605 cm^{-1}) were observed after 24 h of oven time. Interestingly internal silanols (3725 cm^{-1}) were virtually undetectable.

Furthermore, the Lewis acid sites (LAS) and silanols quantification − quantified at respectively 1455cm^{-1} and 4500-4600 cm^{-1} − encountered after 24 h are approximately double as high as in any other sample (Table 2). The latter suggests that the condensed (amorphous) aggregates have a high external surface lacking long-range order. The present Al in these aggregates likely has a LAS contribution. N_2 sorption (Figure 4C) can be used to point out these amorphous aggregates. The samples with the lowest crystallinity (at 16 h and 24 h) indeed show the highest quantities of N_2 sorbed in the higher pressure region (>0.7 p/p_0), which indicates the presence of mesopores and external surface. From BJH and DFT-NL the size of the mesopores of the studied materials was in the range of 20-40 nm. This is likely a quantification of the interstitial space between amorphous matter in accordance with earlier results and literature.[59,76] N_2 sorption in this high pressure region (p/p_0 >0.7) above 30 h is again decreasing (also after 48 h) until virtually no additional sorption is found after 12 days (288 h). The limited external surface or absence of mesopores in solid materials crystallized after 288 h emphasizes the absence of any amorphous particles surrounding the kinetically rough ZSM-5 crystals.

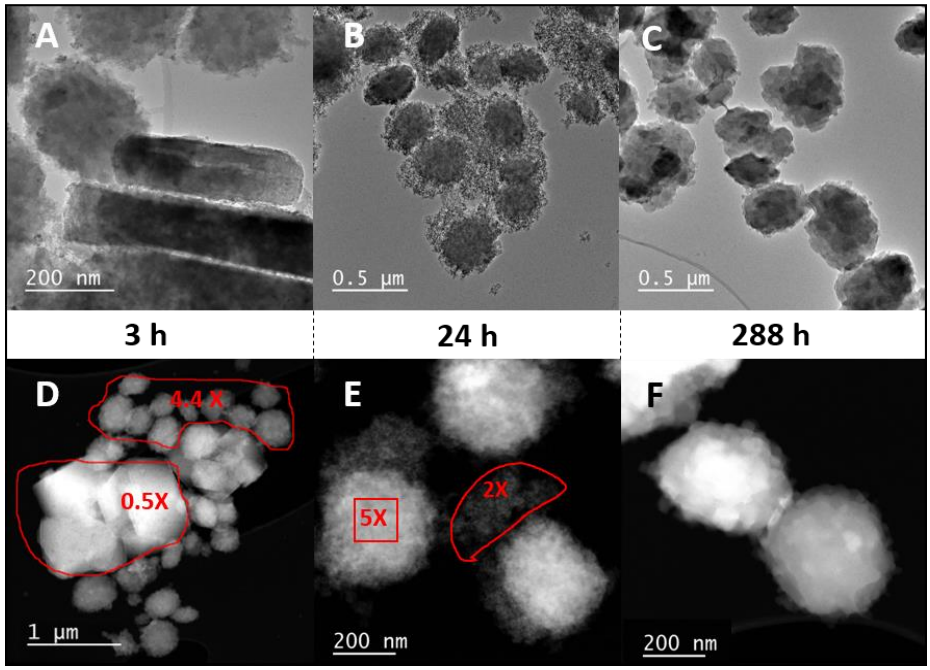

Figure 5. TEM imaging of solids after variable oven times (*[TPA]*^{IZC} series). Heterogeneous particles with different Al contents are localized by EDX mapping. The TEM (A-C) and annular darkfield (ADF) STEM images (D-F) are both representative regions for the full sample (A and D are the same sample, etc). The local Si/Al values detected by EDX in encircled regions (red) are not calibrated to a standard material, but relative to the Si/Al of each sample. The overall Si/Al (ICP-AES) after 3 h, 24 h, and 288 h are 32, 34, and 52, respectively.

From elemental mapping (STEM-EDX, Figure 5D-F), it was observed that the particles with different morphology have a differentSi and Al content, similar as found in other recent work on ZSM-5.[77] The values depicted in Figure 5D-F only allow a relative comparison (no internal calibration). In the 3 h sample, the regions representative for ellipsoidal ZSM-5 crystals demonstrates a Si/Al ratio nine times higher than for the Al rich 'FAU remnants' (Figure 5D, so highly siliceous). A similar output was generated by applying lower synthesis temperatures (100°C) and longer times on identical synthesis mixtures where the mixtures harvested contain large Al-rich FAU remnants and Si-rich amorphous particles (TEM images, Figure S12). Detailed results of low temperature *[TPA]*$^{IZC\text{-}100°C}$ are found in Section S2. Despite the slower pace, the evolution pathway is seemingly temperature-independent in the applied range (100-160°C). From localized elemental mapping at 24 h it can be detected that amorphous fractions are ~2.5 times

more aluminous than the ellipsoidal fractions (Figure 5E). The exclusively present MFI crystals after 288 h do not reveal significant Al concentration gradients (zoning) within one crystal or between neighboring crystals (Figure 5F), although significant inter-particle variance cannot be excluded based on a single STEM-EDX experiment. Additional STEM-EDX experiments were however performed on solids after 3 h and 24 h (data not shown) to confirm the inhomogeneous aluminum contents encountered within the subsequent solid fractions formed during *[TPA]*^{IZC} crystallization. In conclusion, the results point to limited Al framework assembly during TPA^+(only)-based ZSM-5 crystallization (MFI; Si/Al = 40) and to the very slow assembly stage III taking ~44 h in *[TPA]*^{IZC} versus 1 h to 2 h in *[TPA;Na]*^{IZC} or *[TPA]*$^{Am.}$. Potential explanations for the poor performance of this Al-'averse' synthesis (*[TPA]*^{IZC}*)* can be found in the charge compensating behavior of the system (section 4.1) and the generic properties of IZC (section 4.2) in the discussion section.

3.1.3. Comparative study between IZC crystalizing systems (Si/Al = 40).

To the best of our knowledge, the above investigated crystallization system (*[TPA]*^{IZC}) is the first reported IZC crystallization system that is slower in assembly than its amorphous source-based counterpart, despite the swift dissolution and nucleation steps. A more generic understanding of IZC would be a powerful tool to yield synthesis procedures achieving beneficial material characteristics[33] and is currently lacking in literature. Therefore, the two systems at hand, (*[TPA]*^{IZC} and *[TPA;Na]*^{IZC}) yielding ZSM-5 (MFI), are compared to their TMAda containing counterparts (*[TMAda]*^{IZC} and *[TMAda;Na]*^{IZC}) yielding SSZ-13 with the CHA lattice, with special emphasis on the role of Al.

Sodium-containing IZC systems (*[TPA;Na]*^{IZC} and *[TMAda;Na]*^{IZC}) evolve via kinetically similar pathways. Both systems are depicted in Figure S2, with the former system described

extensively in section 3.1.1. Both evolve from Al-rich solids after 1 h of oven time and show significant crystallinity after 1.5 h, concomitant with rising yields and Si/Al ratios. Full crystallinity, as determined by P-XRD, and maximal yields, are obtained before 2 h and 4 h of oven time for respectively for ZSM-5 (MFI) and SSZ-13 (CHA). In both cases, the dry yield is stable at around 60% during prolonged synthesis and the Si/Al ratio is maintained at 35 rendering those zeolites excellent candidates for a comparative investigation of acid site distributions in their framework (section 3.2).

The odd *[TPA]^{IZC}* crystallizing system is compared to the earlier reported *[TMAda]^{IZC}* crystallization system.[24] Both crystallization systems undergo incongruent dissolution and Al densification in the remnant silica sols followed by quick nucleation in the presence of Al rich sols. Both dissolution and nucleation are found 15 minutes later for Na^+-free IZC towards MFI than to CHA (Figure 6). FAU diffraction lines are detected by P-XRD in *[TPA]^{IZC}* during the dissolution and induction stages, while the latter are completely absent in *[TMAda]^{IZC}* equivalents.[24] The equilibrium distribution between solid and liquid phase is established at a slightly higher Si/Al_S ratio (4) and liquid pH (12.5) for *[TPA]^{IZC}* than for *[TMAda]^{IZC}* (Si/Al_S= 3 and pH = 11.7). The origin for the higher Al yield of 45% found in solids during the induction period of *[TMAda]^{IZC}* versus the Al yield of 35% in *[TPA]^{IZC}* is likely due to the ability of OSDA to interact with framework Al.[33] Whilst $TMAda^+$ appears to be small enough to diffuse through the pores of FAU as recently suggested by Zones,[33] the hydrated diameter of TPA^+ is bigger (7.6Å[78]), and thus TPA^+ likely diffuses less easily through the largest micropore openings of FAU (7.35Å),[79] leading to a higher sorption potential of $TMAda^+$ on FAU remnants. The latter is confirmed by higher weight loss in TGA measured on multiple solids obtained after both 15 minutes and 1 h of oven time (data not shown). Adsorbed organic cations can stabilize their local

surroundings by shielding them from hydroxide attack, as occurring during soft alkaline leaching (desilication).[67] Also note the significantly lower liquid phase pH in the $TMAda^+$ (11.7) than in TPA^+ mixtures (12.5). It can be concluded that the subtle differences in OSDA properties (e.g. different charge density (N^+/C ratio), OSDA geometry and flexibility) do have a small impact on the source dissolution and equilibrium distributions (Stages I & II), but this is not in any way comparable to the large impact of the OSDAs in the assembly stage (Stage III).

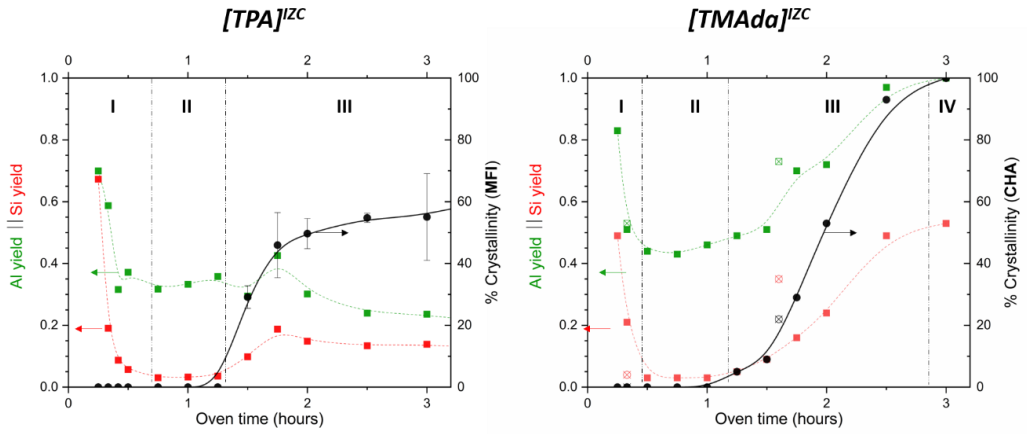

Figure 6. Evolution of MFI and CHA in comparable *[TPA]*^{IZC} and *[TMAda]*^{IZC} systems. The latter system stems from an earlier publication (*Devos et al.*, *Chem Mat.* **2020**).[24]

From the onset of nucleation, CHA nuclei are swiftly evolving to 100% crystalline materials within 2 h after nucleation (3 h overall), whereas crystallization of MFI appears to be halted 45 minutes after nucleation with almost 50% crystallinity (Figure 6, 1.75 h overall). In the fully crystalline CHA (*[TMAda]*^{IZC}- 3h), a solid yield higher than 50% is achieved with complete Al incorporation (Al yield = 1), whereas the abruptly stopped growth in *[TPA]*^{IZC} is followed by a drop in Al yields in the solids. Further (slow) growth coincides with limited assembly of Al into the framework and the formation of (metastable) amorphous aggregates indicating alternative growth pathways (section 3.1.2).

Three of the four investigated systems ([*TMAda]*^{IZC}, *[TMAda;Na]*^{IZC} and *[TPA;Na]*^{IZC}) demonstrate fast sigmoidal crystallization behavior evolving swiftly in a context of Al-rich solids,

whereas assembly of one system (*[TPA]*^{IZC}) is discontinued after the inherently fast nucleation conditions selected here (high Si FAU and high SDA/Si). The deficient growth in *[TPA]*^{IZC} was linked to the lack of framework Al assembly (section 3.1.2.). The key factors to Al incorporation are handled in the discussion section and a generic model for IZC crystallization is established, distinguishing IZC successes based on the tendency of systems to assemble Al into the framework.

3.2. Evaluation of acid sites distribution in IZC via divalent cation capacity (DCC).

These days, further progress in zeolite catalysts requires control over the acid site(s) distribution.[7,19,20,80] Next to acid site control via post-synthetic methods this can also be achieved in-situ during synthesis (as far as consecutive thermal treatments do not alter them greatly).[81,82] However, a detailed understanding of the role of the crystallizing system on the generation of acid sites distribution (or acid-sites genesis, so to say) is lacking. Systematic investigation of the full course of crystallization, e.g. as in section 3.1. provides steppingstones toward understanding synthesis-structure relations linking (IZC) crystallization and the obtained acid site distribution. A commonly used experimental probe method based on aqueous cobalt exchange is exploited to quantify the proximity of acid sites. It can be argued that this is a representative experimental probe for structure-comparing purposes as it is related to catalysis by the fact that hydrated cobalt cations ($[Co(H_2O)_6]^{2+}$) have atomic dimensions close to that of small hydrocarbon reagents or sorbed molecules[41] encountering similar kinetic diffusion barriers on its way to a titratable 'duo' of acid sites. Using the probe method, it is not realistic to just titrate some specific types of local acid sites duo's, commonly assumed to be caused by framework Al (Si_{IV}−OH−Al_{IV}). A 6MR containing two Al across is regarded as the most stable structure for Co^{2+} stabilization, however no 1:1 probe-'acid site duo' is claimed in this work. Especially for the low-symmetry MFI this is important, as it was recently calculated theoretically that numerous (5- or 6-membered rings based) acid site duo's have feasible exchange energies for divalent cobalt.[10]

To validate our probe, we demonstrate the presence of almost solely $Co^{2+}(H_2O)_6$ after room temperature DCC exchange on variable samples. Diffuse reflectance UV-vis absorption spectra (Figure S8) demonstrate the presence of Co^{2+} ions as hexa-aqua complexes (absorption band with a maximum at 19 400 and a shoulder at 20 400 cm^{-1})[83,84] and suggests the absence of significant amounts of cobalt oxides (typically between 25.000-33.000 cm^{-1})[83,85] in both a crystalline sample ($[TPA]^{IZC}$-48h; RC= 83%; Co/Al = 0.08) and a partially amorphous sample from the same series ($[TPA]^{IZC}$-24h; RC= 22%; Co/Al = 0.25). If cobalt oxides species are present, they are not more present in the less crystalline sample.

Moreover, satisfactory saturation of Co^{2+} is achieved after three sequential cobalt exchanges in both MFI and CHA zeolite references (Figure S9), a requirement for equilibrium acid site quantification at room temperature conditions. The amount of cobalt exchanged on a sample is assessed as a Co/Al ratio, or divalent cation capacity (DCC) and is considered as a relative quantification of proximate acid sites or more indirectly, of Al distribution, as most (relevant) acid sites are related to Al.

3.2.1. DCC investigation in partially amorphous zeolite phases: $[TPA]^{IZC}$ and $[TPA]^{Am.}$.

In our earlier work, a decay in divalent cation capacity (DCC) was detected over synthesis time in a fully crystalline SSZ-13 (CHA).[24] Using TPA^+ instead of $TMAda^+$ in the synthesis system $[TPA]^{IZC}$, a similar trend of dropping DCC values with prolonged hydrothermal treatment in the resulting MFI zeolites was found. In contrast, the trend in $[TPA]^{IZC}$ is not unidirectional which reflects the heterogeneous nature of the solids encountered prior to complete crystallization. In Figure 7 the evolution of DCC values is plotted (in gray) against oven time and contains one standard error bars from (2 or 3) synthesis replications. During the first hours of synthesis (1.5 h - 24 h), a sharp rise in DCC is observed. Despite the initial drop in Al content (1.5 h - 2.5 h), the

absolute content of cobalt keeps increasing till it reaches one cobalt cation per 128 T-atoms at 24 h. This corresponds to its highest recorded DCC (Co/Al = 0.27). Later, DCC sharply drops to around 0.07 at 48 h, when full crystallinity is reached, and to even lower DCC values at prolonged synthesis times. A similar observation was done from temporal analysis of calcined microporous materials of the $[TPA]^{Am.}$ series. Pre-crystalline and partially crystalline synthesis solids have a higher DCC then fully crystalline ZSM-5 solids, especially compared to those with prolonged synthesis (Figure 7, red).

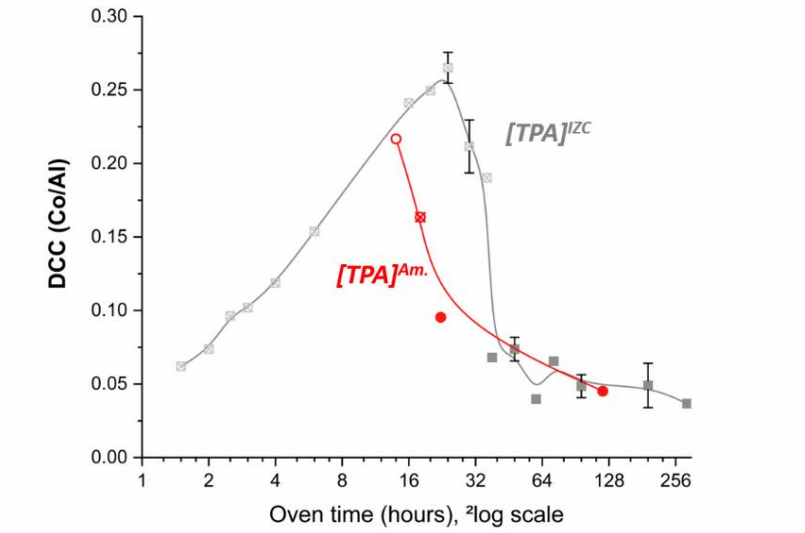

Figure 7. Evolution of the DCC as function of its synthesis time (^{2}log scale) in ZSM-5 from the *[TPA]^{IZC}* (gray squares) and *[TPA]$^{Am.}$* (red dots) crystallizing systems. Cross-filled markers represent partially amorphous samples, non-crystalline samples are represented by open markers. All calcined samples have typical microporosities for ZSM-5.

It is possible to relate the sharp rise and drop of DCC values to the presence of amorphous nanoparticles observed by textural analysis on *[TPA]^{IZC}* samples around 24 h of oven time by TEM (Figure 5B) and N_2 sorption (Figure 4C). In particular from the physisorption data, one can link the additional mesopores to higher DCC values over a large range of oven times. The amorphous nanoparticles, that are suspected to interfere with DCC, were earlier (section 3.1.2.) related to the almost doubling of LAS and Si-OH species (Table 2) in the 24 h sample. Having a DCC (Co/Al = 0.27) that is almost equal to the BAS/Al ratio (0.29, Table 2), it is not possible to match all cobalt

exchange against Bronsted acidic framework Al (Si_{IV}−OH−Al_{IV}) acid site duos. This proves that different acid types contribute to cobalt exchange and point to a significant role of external surface or at least amorphous fractions in cobalt exchange. The latter properties undermine the current interpretation of cobalt exchange as proxy for proximate Si_{IV}−OH−Al_{IV}, but the method does not lose its value in quantifying local acid sites pairs (duo's) or local Al distributions in general. The DCC analysis demonstrated here in the specific *[TPA]^{IZC}* system showcases the complexity of both simple divalent cation exchange and of synthesized (non-ideal) zeolitic materials containing solid precursors and amorphous parts. Even though the diverse nature of exchange sites probed by cobalt require additional characterization before in-depth interpretation, DCC analysis can be regarded as a powerful tool to systematically review the outcome of synthesis processes in detail, as demonstrated below.

3.2.2. DCC evolution in mature ZSM-5 (MFI) and SSZ-13 (CHA) containing sodium.

Ideally, an investigation on the temporal evolution of DCC requires most physicochemical properties to remain identical in the crystallizing system −i.e. Si/Al ratios, identical yields, external surface, acid site content, …− given the detected limitations on DCC evaluation in partially amorphous solids. Surprisingly, two crystallization systems apparently meet these tight requirements: *[TPA;Na]^{IZC}* and *[TMAda;Na]^{IZC}*, as they are identical in input, crystallization behavior, and output, apart from the OSDA used and the framework type formed (section 3.1.3).

The temporal evolution of DCC values for fully crystalline zeolites from *[TPA;Na]^{IZC}* (black) and *[TMAda;Na]^{IZC}* (green) is plotted in Figure 8. In *[TPA;Na]^{IZC}* synthesis, DCC drops substantially with time, from a Co/Al ratio of 0.19 at 2 h to 0.06 at 288 h (12 days). In the first 6 h, this decay, in the log plot, occurs very rapid, and slows down as the synthesis continues. TEM-EDX measurements (Figure S3) demonstrate that both Al and Co are homogeneously distributed

over the zeolite crystal and FT-IR demonstrates a similar distribution of acid types (Table 1). Because less silanols (Si-OH) were quantified in the 2 h sample than in its 4 days counterpart with much lower DCC, the majority of the counterbalanced acid sites for cobalt that vanish are considered to contain Al. As such, it is expected that migration of aluminum takes place (see discussion in section 4.4) to explain the depletion of local proximate acid site with prolonged synthesis in the crystalline MFI containing sodium (*[TPA;Na]^{IZC}*).

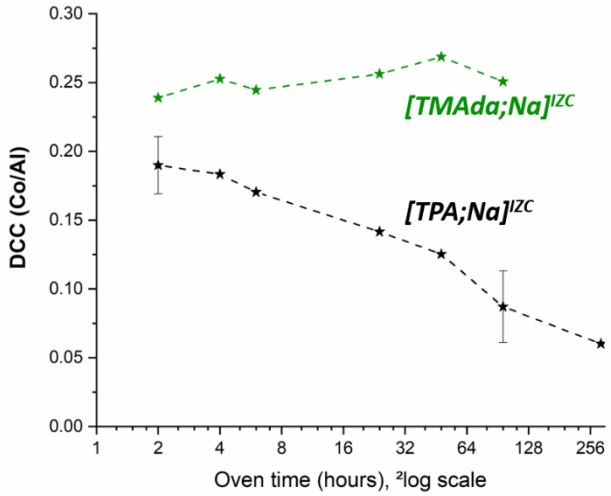

Figure 8. Evolution of DCC (Co/Al) as function of its synthesis time in mature highly crystalline ZSM-5 (MFI) from *[TPA;Na]^{IZC}* and SSZ-13 (CHA) from *[TMAda;Na]^{IZC}* synthesis systems. The error bar at 2 and 96 h considers three and two full synthesis replicas, respectively.

In contrast, no drop in DCC is observed in the CHA framework (Co/Al = 0.25) in the case of *[TMAda;Na]^{IZC}* syntheses (Figure 7; green). The stable acid site distribution with synthesis prolongation is likely the result of the framework geometry and SDA encagement (both $TMAda^+$ and Na^+) as explained in the discussion below (section 4.4). The DCC of the FAU (CBV780) parent is Co/Al = 0.18 (Si/Al=40). These values are very similar to the output MFI and CHA at low synthesis times. This could be an indication that the high DCC potential is already present in the parent materials. However, there is much doubt if the initial DCC plays a determining role after all, as inherent Al densification is observed during FAU dissolution (see below in discussions).

4. Discussion:

4.1. Importance of charge balancing during zeolite assembly

The lack of growth prolongation in sodium free MFI systems (*[TPA]^{IZC}*) can be linked to the limited framework assembly (insertion) of Al (section 3.1.2). The latter does not seem to be a problem in the other investigated equimolar IZC synthesis systems (*[TPA;Na]^{IZC}, [TMAda]^{IZC}*, or *[TMAda;Na]^{IZC}).* The importance of three specific aspects of zeolite synthesis on framework Al incorporation are revisited below to understand the intrinsic differences between the synthesis systems: (I) topology specific Al preference, (II) siting of SDA^+ charge compensators, (III) the nature of SDA^+ charge compensators, and (IV) the combination effect of multiple SDAs.

A first element influencing Al incorporation is the intrinsic stability of certain topologies (I). It is long known that some topologies are preferably Al-rich by nature (e.g. LTA or FAU) and others are Si-rich, such as MFI. The latter is backed by computational results on idealized topologies. The lowest relative framework energies for MFI topology are found in high Si/Al regions, while at Si/Al ≤ 3 for CHA.[18] This effect most likely stems from the intrinsic bond angles stability of Si−O−Al and Si−O−Si,[86] and explains the high tendency for Al assembly in CHA crystallizing zeolites. The SDAs used to crystallize zeolites do not only have a space filling role, they also serve in charge compensation. Steric hinderance will nonetheless limit the amount of charge compensation centers (II). For example, MFI can accommodate 8-10 Na^+ whereas only 4 TPA^+ cations can be incorporated per unit cell.[87] As such, more charge is provided to compensate framework Al if smaller cations are used. The latter is clearly observed in MFI crystallization. The system using Na^+ (*[TPA;Na]^{IZC}*) achieves a higher Al-yield (70%) than *[TPA]^{IZC}* (≤ 60%). Note the inverse trend in CHA crystallizing systems, as [*TMAda]^{IZC}* achieves ~100% Al yield versus 70% in *[TMAda;Na]^{IZC}*. This underlines the specific tendency of Al incorporation in each

'framework-SDA' system. Not only the quantity and SDA size play a role, also the nature of the charge balancing (III) may be an important factor. Next to framework Al ($[AlO_{4/2}]^-$), cationic SDA charge can also compensate other anionic (acid) charges in synthesized SDA/framework composites such as extra-framework aluminum or silanol defects. The shielding effect of the propyl branches of TPA^+ (with a central charge) may cause (weak) charge compensation specifically against silanol anionic charge (defects), whereas the less-shielded asymmetric $TMAda^+$ (with the charge on one side of the molecule) provokes a stronger electrostatic (coulomb-type) charge compensation more suitable to compensate strong acidic framework Al. In this respect, sodium will have the strongest electrostatic (coulombic) charge compensation towards framework Al, as it its charge is not at all shielded by alkyl moieties. Small inorganic SDAs such as Na^+ combine a high availability (siting) and low shielding (nature) which fortifies its effect to assemble framework Al (high charge density). Finding the right combination (IV) of high charge density and low charge density cations is a promising route to open up new synthesis routes such as demonstrated using *'dual templating'* and *Charge Density Mismatch (CDM)* concepts.[25,88] In the IZC work here, an MFI crystallization was successful using a combination of TPA^+ and Na^+ where the sodium-free counterpart was not (section 3.1).

The above described determining factors for Al charge balancing are postulated here to be key in understanding and tailoring the performance of IZC synthesis systems (see below, section 4.2), or other crystallization systems (seeded systems), and to tweak Al distributions (section 4.5) based on synthesis.

4.2. Generic model for IZC assembly

A generic understanding of IZC would be a valuable tool to design synthesis procedures with beneficial zeolite characteristics.[33] To the best of our knowledge, this is the first comprehensive

model for IZC type syntheses with generic features. Provided appropriate dissolution conditions (~pH, SDA, and zeolitic source), the proposed model assigns heterogeneous nucleation in an aluminous environment as key phenomena provoking the swift nucleation occurring in this system. The model further relies heavily on the role of Al within the crystallizing mixture (Al-'loving' and Al-'averse' systems) and also contains clues for Al-distribution control at the nanometer scale. It is based on observations from systematic investigation of high silica (Si/Al = 40) IZC (*FAU-to-CHA* and *FAU-to-MFI)* in time as described above (3.1), literature, our previous work[24] and some conjectures.

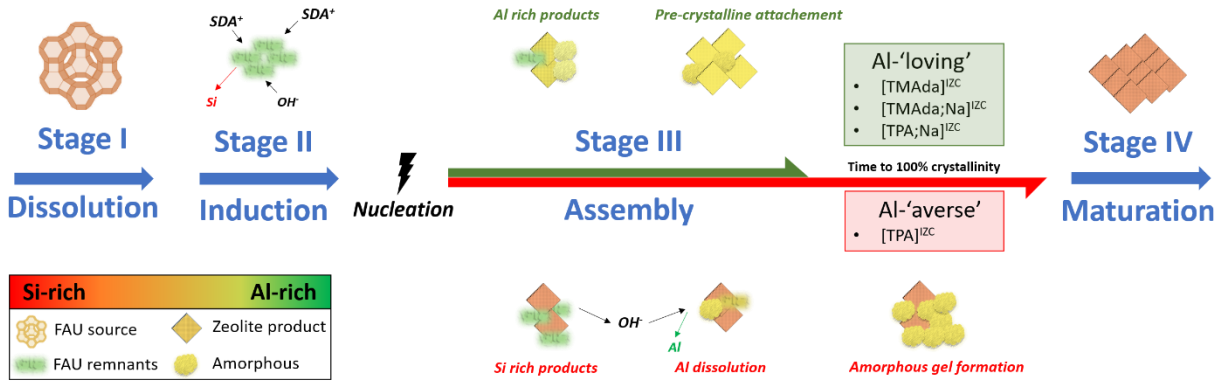

Scheme 1. A comprehensive model for the evolution of solid stages over the course of IZC with generic features. Fast nucleation occurs intrinsically due to the Al dense context (attracting OSDAs). Synthesis systems avoiding Al assembly (Al-'averse') need to change in assembly mode (encountering metastable intermediates) and are much slower in assembly.

Inherently, hydrothermal treatment of an organic OSDA and a zeolitic source in highly alkaline conditions causes incongruent dissolution and Al densification via reversible (de)polymerization due to the higher stability of Si−O−Al than Si−O−Si bonds in alkaline media.[89] It is supposed that −at least on the nanoscale− a fraction of the crystallinity of the source is maintained by the protection of local adsorbed OSDA (FAU remnants in Scheme 1). OSDA exchange (or adsorption) proportional to the Al content was recently identified by Zones *et al.* as a crucial factor determining IZC synthesis.[33] Hence, the inherent Al rich nature of the solids enables the system to quickly

attract the necessary amount of OSDAs. The latter is important for the swift creation of viable nuclei as nucleation is suspected to occur at the liquid-solid interface.[69,90,91] Another factor that is likely responsible for the lower kinetic barriers for IZC nucleation is heterogeneous nucleation. Solid residues non-selectively act as 'seeds' lowering the energetic barriers for viable nuclei.[37] Provided some structural similarity between the source and final zeolite, so called '*nanoparts*', the heterogeneous nucleation is selective (crystalline seeding). However, solid evidence for these particles is missing[25,27,28] and recent works postulates that structural similarity is not an important prerequisite for successful IZC transformations.[30,31]

After the point of nucleation, the assembly conditions are largely in the hands of the combination of SDAs and the forming framework as put forward in section 4.1. The available (Al-rich) context after IZC nucleation requires crystallizing conditions that easily facilitates the incorporation of Al (Al-'loving') for fast IZC assembly (green line Scheme 1), while growth of Al-'averse' IZC systems will be limited (or even halted). Note that only the $[TPA]^{IZC}$ from the present study is categorized as 'Al'-averse. The three other IZC systems, as well as the majority of IZC synthesis systems are expected to be 'Al-loving'. The specific mechanism of assembly in both Al-'loving' and Al-'averse' systems remain very elusive. However, there are some clues that could explain why certain reaction mechanisms are either fast or slow in the context starting from Al-rich sols. For example, one phenomenon that may take place during assembly in Al-'loving' systems is the formation of pre-crystalline amorphous fractions prior to complete crystallization (pre-crystalline attachment, Scheme 1).[66,75] In the context of Al-'averse' syntheses, the assembly comes to a halt despite fast nucleation (Scheme 1, red line). Perhaps, this can be due to excess non-incorporated Al at assembling locations impeding growth in these regions. Growth of the first assembled fractions also release OH^- (Scheme 1), which may trigger leaching of non-framework Al away

from the solid (Al yield drop in Figure 3A), hereby lowering SDA attraction in the assembling region and promoting polycondensation of colloidal Si-SDA species in the liquid phase,[89] which provokes their aggregation.[92] Such formation of metastable amorphous gel intermediates may lower the concentration of available species (supersaturation) and ultimately require another (slow) growth mode to take place.

In summary, a comprehensive model for IZC synthesis is proposed comparing different crystallization systems starting from similar batch compositions. Syntheses show very little fundamental differences in evolution prior to nucleation (Stages I and II) due to the inherent dissolution and nucleation properties of the IZC system, condensing SDAs at the dissolving Al-rich surface. After the fast nucleation, the success of assembly is presumed to largely depend on the affinity of the crystalline system for framework Al as demonstrated by the distinction of seemingly generic 'Al-averse' and Al-'loving' crystallizing systems (Scheme 1, red and green lines respectively).

4.3. Defining the DCC probing parameter and practical applications

It is important to understand the speciation of the acid sites counterbalancing cobalt cations, i.e. $[Co(H_2O)_6]^{2+}$, the actual form of exchanged cobalt at room temperature. By investigating DCC on partially crystalline ZSM-5 materials in the *[TPA]^{IZC}* and *[TPA]$^{Am.}$* series (section 3.2.1), it is now demonstrated that amorphous fractions are also selective to cobalt uptake. Cobalt exchange is not just limited to strong internal bridging Si_{IV}−OH−Al_{IV} hydroxyls, which broadens the interpretation of typical cobalt cation exchange as proxy for acid sites distribution. The latter finding is endorsed by the recent publication of Chen and co-workers.[41] Using divalent cation exchange (Ca^{2+}, Cu^{2+}, Ba^{2+}) coupled with ^{1}H MAS NMR they measured the contribution of extra-framework amorphous Al (Bronsted acidic extra-framework aluminols) to divalent cation exchange allowing them to

probe its synergistic effect on catalysis. As such, the quantification of DCC contains more diverse information than the classical interpretation of divalent cation exchange as a proxy for local Al inter-distance (or distribution). The awareness of the probes exchange ability towards (partially-) amorphous and extra-framework acid sites enables us to use DCC to easily quantify complex phenomena experimentally via a simple technique (ion exchange). The latter is not always possible using direct and complex characterization methods (e.g. the presence of '*NMR invisible'* Al species in dehydrated MFI[93–95]).

4.4. The importance of prolonged synthesis on acid site distribution.

Our earlier report detailing an extensive synthesis parameter screening for *[TMAda]*^{IZC} revealed the importance of kinetically fast growth to achieve zeolites with high DCC.[24] IZC was identified as promising synthesis route for materials requiring proximate acid sites, as proven for methane partial oxidation in SSZ-13. However, the high DCC potential is not always maintained with prolonged synthesis duration. The DCC drop in time observed in most investigated synthesis systems here (section 3.2) is expected to be caused by the depletion of proximate Al acid sites. The latter is backed by the thermodynamic charge balancing perspective as two Al tetrahedra are electrostatically repulsive, causing strain, in line with Dempsey's Rule of (Al) charge separation.[17] Provided some flexibility of the formed framework, it is believed that energetic barriers are sufficiently low to mobilize Al (and counterions) in most synthesis systems, especially when non-framework Al is involved. The TGA data of *[TPA;Na]*^{IZC} and other synthesis system demonstrates that as-made materials with short oven time (2 h) do have a higher flexibility than their equivalents with more prolonged oven time (96 h), as derivative thermogravimetric (DTG) peaks shift to higher temperatures with time (section 3.1.1). Hence, changes in the internal stabilization of SDA-frameworks composites take place, from which we deduce the mobility of charged species towards

higher thermodynamic stability. The latter is possible as zeolite assembly is a sum of numerous kinetically reversible non-covalent interactions.[96,97] Gallium mobility via intra-framework migration,[98] Si island forming in silicoaluminophosphates,[99] and Al mobility in multiple works on Al zoning.[100–102] are literature examples of framework atom mobility during hydrothermal synthesis, justifying our presumption of T-atom mobility to explain the DCC drops in this and earlier work.[24]

The alleged T-atom migration phenomena does not seem to occur in Na^+ containing CHA zeolites (*[TMAda;Na]*^{IZC}), as no drop in DCC was observed over time. In the latter case, the as-synthesized frameworks preferentially stabilize Na^+ inside a *d6r* and $TMAda^+$ in the *cha*-cage (Scheme 2).[13] It can be inferred that the strongly encaged cations limit the mobility of the proximate anionic charges disabling their charge separation as visualized in Scheme 2 (top). In Scheme 2 only framework Al is represented for simplicity, but other anionic charges may also be involved such as silanol or aluminols. In contrast to the latter CHA system, the Na^+ containing MFI does not encounters high energetic barriers to separate these proximate anionic charges due to less confined charges. The stabilization energies of multiple 6MR's for Na^+ are not significantly different and the TPA molecule is more flexible within its void space. Additionally, the intrinsically lower tendency to contain Al in MFI may be another contributor to ease the mobility of aluminum and related acid sites (Scheme 2, bottom).

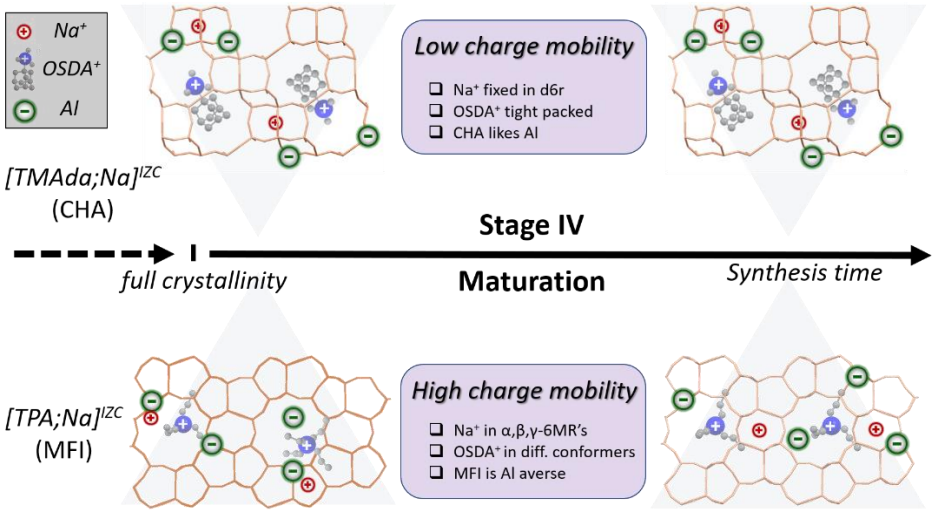

Scheme 2: Potential mechanisms of acid site (re-)distribution in Na-containing CHA (top) and MFI (bottom) zeolite synthesis during prolonged hydrothermal synthesis (maturation, Stage IV). Both anionic charge related to framework and non-framework Al are depicted as 'Al'.

4.5. Understanding genesis and evolution of acid site arrangements during synthesis

It has long been known that post-treatments influence Al[103–108] and thus acid site distributions providing a facile route to modify zeolites towards more optimal synthesis-structure relations. More recently, the zeolite catalysis community has begun exploring the potential of acid site distributions tuned by the underlying synthesis, hereby enlarging the toolbox to shape fine-tuned zeolites for applications. Nonetheless, a rational understanding of the creation of acid site arrangements during synthesis is lacking due to the complex nature of the crystallization process, the seemingly endless amount of proximate Al and acid site possibilities (even in very symmetric frameworks such as CHA[109]) and the lack of systematic and comparable syntheses.

Based on the distinct crystallization pathways of the various investigated syntheses in this work (3.1) and the direct probing of local Al and other negative charge density via DCC analysis (3.2), we would like to point out three different factors of zeolite synthesis with a pivotal role on the genesis of acid site distributions and further evolution during maturation: (I) charge balance between the SDA cations and anionic framework charge, (II) the specific nucleation and assembly

kinetics, and (III) internal rearrangement of cations and negative framework charge during maturation stages.

In line with most published reports on acid site distribution and Al distribution, we were able to derive the importance of (charge) SDA stabilization within different frameworks (I). Notably in *[TPA;Na]*^{IZC} and *[TMAda;Na]*^{IZC} synthesis systems, the charge balancing role of the SDA combinations inside the specific framework confinements are recognized to yield thermodynamically-driven acid site (Al) distributions deflecting from random arrangements (section 3.2.2). However, this is not sufficient to explain the recent observations of more Al dense regions in (FAU-to-CHA) IZC,[24,40] in comparison with synthesis from amorphous sources.[12,24]

Therefore, a second influence on Al (acid site) distribution was proposed, based on fast growth kinetics: the role of nucleation and assembly pathways (II), as suggested from the earlier work of our group on FAU-to-CHA (*[TMAda]*^{IZC}).[24] From the generic model proposed for IZC evolution (section 4.2, Scheme 1), and literature, it can be suggested that specific Al dense regions may persist throughout the evolution[40] and rationalized that fast crystallization kinetics (e.g. Al-'loving' IZC systems, 4.1.) are beneficial to create (or maintain) these Al rich regions into high proximate acid site densities, i.e. kinetically-captured proximate Al distributions.[24]

In addition to that, a last phenomenon (III) influencing acid site distribution was proposed by linking flexibility of the SDA-framework (= often an inorganic-organic hybrid[96,97]) complex to dropping DCC values as discussed in section 4.4.: thermodynamically-driven internal rearrangement of ionic charge with prolonged synthesis (maturation) in line with Dempsey's rule.[17] The latter is believed to occur exclusively in frameworks allowing sufficient charge mobility (Scheme 2).

5. Conclusion:

The nature of IZC and the internal distribution of Al and acid sites in resulting ZSM-5 (MFI) and SSZ-13 (CHA) zeolites were unraveled by investigating the evolution of IZC in several crystallization systems with the same batch composition (SiO_2: 0.025Al: 0.35 SDA^+: 0.35OH^- :12.5H_2O), two variations of source materials (crystalline vs. amorphous sources), and two combinations of SDA compositions at a constant cationic charge (($OSDA^+ + Na^+$)/Al = 14).

Interzeolite conversion (IZC) propels fast nucleation in any OSDA-zeolite system, and excels as a synthesis strategy (fast and high yield) when performed in Al-'loving' crystallizing environments, such as systems containing sodium (*[TPA;Na]*^{IZC} and *[TMada;Na]*^{IZC}) or forming Al-keen frameworks such as CHA (*[TMAda]*^{IZC}). However, in Al-'averse' crystallizing systems (*[TPA]*^{IZC}, Scheme 1), the fast nucleation inherent to IZC is not followed by swift crystallization (growth), to the point that full crystallization is achieved twice faster in its amorphous counterpart synthesis system (*[TPA]*$^{Am.}$). Growth hinder likely stems from the requirement for a secondary growth mechanism via classical gel formation while part of the sources are already consumed. Al-averse systems seem to be halted after nucleation and switch to a gel-like phase before slowly continuing, hereby losing the kinetic advantages of IZC. From these observations, the importance of charge balancing during assembly was discussed (4.1) and a generic model for IZC evolution was presented (4.2), with the potential to tailor future generations of IZC zeolite catalysts.

DCC quantification, in form of the saturation uptake of aqueous divalent cobalt, was exploited to probe local acid site (anionic charge) distributions. By analyzing DCC all throughout the *[TPA]*^{IZC} system, the probed acid sites are clearly not limited to typical Si_{IV}−OH−Al_{IV}. This expands the interpretation of the DCC method from Al distributions to acid site distributions in general, enabling us to easily quantify, to some extent, synergistic (partially-) amorphous and non-

framework acid sites.[41] Combining the temporal synthesis evolutions and DCC, three phenomena regulating the genesis of final acid site distributions are discerned: (I) charge balancing between the SDA cations and anionic framework charges, (II) crystallization kinetics allowing thermodynamically less-favorable (metastable) charge distributions and (III) framework charge mobility allowing a degree of internal rearrangement of cations and acid sites (thus T-atoms) during maturation stages. While the first two phenomena were described earlier in literature, the last phenomenon, quite novel, is emphasized here. Relations were found between prolonged hydrothermal treatment and the extent of framework charge mobility across several synthesis systems by DCC quantification. These changes, which occur mostly after full crystallization as defined by XRD is reached, profoundly impact the Al- and acid distributions. The length of a synthesis can thus be crucial, and harbor a lot of impact on the catalytic and ion-exchange properties, even though X-ray and pore volume data would suggest the zeolite crystallization is finished. Stopping a mature synthesis early or late, can thus be directly exploited for catalytic effects.

Although further investigation is required to entangle specific synthesis-structure relations useful for catalysis, the principles and learnings on the decisive role of Al in IZC systems seem generic. Also, it can be suggested that more flexible (e.g. occluded OSDA burn-off at lower temperatures than usual) as-made materials contain a higher content of defective sites (e.g. silanols or non-framework Al), given the TGA correlation with DCC. In this light, the (semi-) quantitative DCC probe is a powerful and convenient tool to achieve a better understanding of the phenomena behind acid site (re)distribution during synthesis. The principles laid out here open the door for tailoring zeolites to catalysis, in particular for redox zeolite catalysis which often relies on a divalent cation exchange stage in their preparation.

ASSOCIATED CONTENT

Supporting Information.

This document contains additional characterization: XRD diffractograms, nitrogen sorption isotherms, , additional TEM-images, STEM-EDX mappings of metal containing zeolites, yield and crystallinity data (*[TPA;Na]^{IZC}* and *[TMAda;Na]^{IZC}*), details on divalent cation exchange (DCC) quantification by cobalt exchange (DR-UV−vis spectra) and additional sections on *[TPA]$^{Am.}$* and *[TPA]$^{IZC\text{-}100°C}$*·syntheses (PDF).

AUTHOR INFORMATION

Corresponding Author

* M.D.: michiel.dusselier@kuleuven.be

Author Contributions

J.D. and M.D. designed the research. J.D., S.R., I.K. and C.V. performed experiments. J.D., S.R, I.K. and M.D. analyzed the data. J.D. and M.D. wrote the manuscript with input of all authors.

Funding Sources

J.D., S.R., C.V.G.,I.K. and M.D. thank the Research Foundation - Flanders (FWO Vlaanderen) for funding (Grants G0C1618N and G085220N to M.D, 12ZQ420N to C.V.G. and 1260321N to I.K.). The authors are grateful to the Hercules Foundation for financing the TEM (AKUL/13/19).

Notes

The authors declare no competing financial interests.

ACKNOWLEDGMENT

SACHEM is explicitly thanked for providing the organic structure directing agents (TMAda-OH and TPA-OH).

REFERENCES

(1) Yang, C. T.; Janda, A.; Bell, A. T.; Lin, L. C. Atomistic Investigations of the Effects of Si/Al Ratio and Al Distribution on the Adsorption Selectivity of n-Alkanes in Brønsted-Acid Zeolites. *J. Phys. Chem. C* **2018**, *112*, 9397–9410.

(2) Sazama, P.; Dědeček, J.; Gábová, V.; Wichterlová, B.; Spoto, G.; Bordiga, S. Effect of Aluminium Distribution in the Framework of ZSM-5 on Hydrocarbon Transformation. Cracking of 1-Butene. *J. Catal.* **2008**, *254*, 180–189.

(3) Sazama, P.; Wichterlova, B.; Dedecek, J.; Tvaruzkova, Z.; Musilova, Z.; Palumbo, L.; Sklenak, S.; Gonsiorova, O. FTIR and 27Al MAS NMR Analysis of the Effect of Framework Al- and Si-Defects in Micro- and Micro-Mesoporous H-ZSM-5 on Conversion of Methanol to Hydrocarbons. *Microporous Mesoporous Mater.* **2011**, *143*, 87–96.

(4) Yu, Z.; Li, S.; Wang, Q.; Zheng, A.; Jun, X.; Chen, L.; Deng, F. Brønsted/Lewis Acid Synergy in H-ZSM-5 and H-MOR Zeolites Studied by 1H and 27Al DQ-MAS Solid-State NMR Spectroscopy. *J. Phys. Chem. C* **2011**, *115*, 22320–22327.

(5) R. Di Iorio, J.; T. Nimlos, C.; Gounder, R. Introducing Catalytic Diversity into Single-Site Chabazite Zeolites of Fixed Composition via Synthetic Control of Active Site Proximity. *ACS Catal.* **2017**, *7*, 6663–6674.

(6) Bernauer, M.; Tabor, E.; Pashkova, V.; Kaucký, D.; Sobalík, Z.; Wichterlová, B.; Dedecek, J. Proton Proximity – New Key Parameter Controlling Adsorption, Desorption and Activity in Propene Oligomerization over H-ZSM-5 Zeolites. *J. Catal.* **2016**, *344*, 157–172.

(7) Chizallet, C. Toward the Atomic Scale Simulation of Intricate Acidic Aluminosilicate Catalysts. *ACS Catal.* **2020**, *10*, 5579–5601.

(8) Yokoi, T.; Mochizuki, H.; Namba, S.; Kondo, J. N.; Tatsumi, T. Control of the Al Distribution in the Framework of ZSM-5 Zeolite and Its Evaluation by Solid-State NMR Technique and Catalytic Properties. *J. Phys. Chem. C* **2015**, *119*, 15303–15315.

(9) Muraoka, K.; Chaikittisilp, W.; Yanaba, Y.; Yoshikawa, T.; Okubo, T. Directing Aluminum Atoms into Energetically Favorable Tetrahedral Sites in a Zeolite Framework by Using Organic Structure-Directing Agents. *Angew. Chemie Int. Ed.* **2018**, *57*, 3742–3746.

(10) Nimlos, C. T.; Hoffman, A. J.; Hur, Y. G.; Lee, B. J.; Di Iorio, J. R.; Hibbitts, D. D.; Gounder, R. Experimental and Theoretical Assessments of Aluminum Proximity in MFI Zeolites and Its Alteration by Organic and Inorganic Structure-Directing Agents. *Chem. Mater.* **2020**, *32*, 9277–9298.

(11) Hur, Y. G.; Kester, P. M.; Nimlos, C. T.; Cho, Y. R.; Miller, J. T.; Gounder, R. Influence of

Tetrapropylammonium and Ethylenediamine Structure-Directing Agents on the Framework Al Distribution in B-Al-MFI Zeolites. *Ind. Eng. Chem. Res.* **2019**, *58*, 11849–11860.

(12) Di Iorio, J. R.; Gounder, R. Controlling the Isolation and Pairing of Aluminum in Chabazite Zeolites Using Mixtures of Organic and Inorganic Structure-Directing Agents. *Chem. Mater.* **2016**, *28*, 2236–2247.

(13) Di Iorio, J. R.; Li, S.; Jones, C. B.; Nimlos, C. T.; Wang, Y.; Kunkes, E.; Vattipalli, V.; Prasad, S.; Moini, A.; Schneider, W. F.; Gounder, R. Cooperative and Competitive Occlusion of Organic and Inorganic Structure-Directing Agents within Chabazite Zeolites Influences Their Aluminum Arrangement. *J. Am. Chem. Soc.* **2020**, *142*, 4807–4819.

(14) Feijen, E. J. P.; Lievens, J. L.; Martens, J. A.; Grobet, P. J.; Jacobs, P. A. Silicon and Aluminum Ordering in Frameworks of FAU and EMT Aluminosilicate Zeolites Crystallized in the Presence of Crown Ethers. *J. Phys. Chem.* **1996**, *100*, 4970–4975.

(15) Biligetu, T.; Wang, Y.; Nishitoba, T.; Otomo, R.; Park, S.; Mochizuki, H.; Kondo, J. N.; Tatsumi, T.; Yokoi, T. Al Distribution and Catalytic Performance of ZSM-5 Zeolites Synthesized with Various Alcohols. *J. Catal.* **2017**, *353*, 1–10.

(16) Löwenstein, W. The Distribution of Aluminum in the Tetrahedra of Silicates and Aluminates. *Am. Mineral.* **1954**, *39*, 92–96.

(17) Dempsey, E.; Kühl, G. H.; Olson, D. H. Variation of the Lattice Parameter with Aluminum Content in Synthetic Sodium Faujasites. Evidence for Ordering of the Framework Ions. *J. Phys. Chem.* **1969**, *73*, 387–390.

(18) Muraoka, K.; Chaikittisilp, W.; Okubo, T. Energy Analysis of Aluminosilicate Zeolites with Comprehensive Ranges of Framework Topologies, Chemical Compositions, and Aluminum Distributions. *J. Am. Chem. Soc.* **2016**, *138*, 6184–6193.

(19) Wang, S.; He, Y.; Jiao, W.; Wang, J.; Fan, W. Recent Experimental and Theoretical Studies on Al Siting/Acid Site Distribution in Zeolite Framework. *Curr. Opin. Chem. Eng.* **2019**, *23*, 146–154.

(20) C. Knott, B.; T. Nimlos, C.; J. Robichaud, D.; R. Nimlos, M.; Kim, S.; Gounder, R. Consideration of the Aluminum Distribution in Zeolites in Theoretical and Experimental Catalysis Research. *ACS Catal.* **2018**, *8*, 770–784.

(21) Dědeček, J.; Sobalík, Z.; Wichterlová, B. Siting and Distribution of Framework Aluminium Atoms in Silicon-Rich Zeolites and Impact on Catalysis. *Catal. Rev. - Sci. Eng.* **2012**, *54*, 135–223.

(22) Pashkova, V.; Klein, P.; Dedecek, J.; Tokarová, V.; Wichterlová, B. Incorporation of Al at ZSM-5 Hydrothermal Synthesis. Tuning of Al Pairs in the Framework. *Microporous Mesoporous Mater.* **2015**, *202*, 138–146.

(23) Dědeček, J.; Tabor, E.; Sklenak, S. Tuning the Aluminum Distribution in Zeolites to Increase Their Performance in Acid-Catalyzed Reactions. *ChemSusChem* **2019**, *12*, 556–576.

(24) Devos, J.; Bols, M. L.; Plessers, D.; Goethem, C. Van; Seo, J. W.; Hwang, S. J.; Sels, B. F.; Dusselier, M. Synthesis–Structure–Activity Relations in Fe-CHA for C–H Activation: Control of Al Distribution by Interzeolite Conversion. *Chem. Mater.* **2020**, *32*, 273–285.

(25) Dusselier, M.; Davis, M. E. Small-Pore Zeolites: Synthesis and Catalysis. *Chem. Rev.* **2018**, *118*,

5265–5329.

(26) Deneyer, A.; Ke, Q.; Devos, J.; Dusselier, M. Zeolite Synthesis under Nonconventional Conditions: Reagents, Reactors, and Modi Operandi. *Chem. Mater.* **2020**, *32*, 4884–4919.

(27) Honda, K.; Itakura, M.; Matsuura, Y.; Onda, A.; Ide, Y.; Sadakane, M.; Sano, T. Role of Structural Similarity between Starting Zeolite and Product Zeolite in the Interzeolite Conversion Process. *J. Nanosci. Nanotechnol.* **2013**, *13*, 3020–3026.

(28) Li, C.; Moliner, M.; Corma, A. Building Zeolites from Precrystallized Units: Nanoscale Architecture. *Angewandte Chemie - International Edition*. Wiley-VCH Verlag November 19, 2018, pp 15330–15353.

(29) Itabashi, K.; Kamimura, Y.; Iyoki, K.; Shimojima, A.; Okubo, T. A Working Hypothesis for Broadening Framework Types of Zeolites in Seed-Assisted Synthesis without Organic Structure-Directing Agent. *J. Am. Chem. Soc.* **2012**, *134*, 11542–11549.

(30) Jain, R.; Rimer, J. D. Seed-Assisted Zeolite Synthesis : The Impact of Seeding Conditions and Interzeolite Transformations on Crystal Structure and Morphology. *Microporous Mesoporous Mater.* **2020**, *300*, 110174.

(31) Schwalbe-Koda, D.; Jensen, Z.; Olivetti, E.; Gómez-Bombarelli, R. Graph Similarity Drives Zeolite Diffusionless Transformations and Intergrowth. *Nat. Mater.* **2019**, *18*, 1177–1181.

(32) Qin, W.; Jain, R.; Robles Hernández, F. C.; Rimer, J. D. Organic-Free Interzeolite Transformation in the Absence of Common Building Units. *Chem. - A Eur. J.* **2019**, *25*, 5893–5898.

(33) Zones, S. I.; Lew, C. M.; Xie, D.; Davis, T. M.; Schmidt, J. E.; Saxton, R. J. Studies on the Use of Faujasite as a Reagent to Deliver Silica and Alumina in Building New Zeolite Structures with Organo-Cations. *Microporous Mesoporous Mater.* **2020**, *300*, 110162.

(34) Goel, S.; Zones, S. I.; Iglesia, E. Synthesis of Zeolites via Interzeolite Transformations without Organic Structure-Directing Agents. **2015**, *27*, 2056–2066.

(35) Piccione, P. M.; Laberty, C.; Yang, S.; Camblor, M. A.; Navrotsky, A.; Davis, M. E. Thermochemistry of Pure-Silica Zeolites. *J. Phys. Chem. B* **2000**, *104*, 10001–10011.

(36) Petrovic, I.; Navrotsky, A.; Davis, M. E.; Zones, S. I. Thermochemical Study of the Stability of Frameworks in High Silica Zeolites. *Chem. Mater.* **1993**, *5*, 1805–1813.

(37) Li, R.; Chawla, A.; Linares, N.; Sutjianto, J. G.; Chapman, K. W.; Martínez, J. G.; Rimer, J. D. Diverse Physical States of Amorphous Precursors in Zeolite Sol Gel Syntheses. *Ind. Eng. Chem. Res.* **2018**, *57*, 8460–8471.

(38) Liang, Y.; J. Jacobson, A.; D. Rimer, J. Strontium Ions Function as Both an Accelerant and Structure-Directing Agent of Chabazite Crystallization. *ACS Mater. Lett.* **2021**, *0*, 187–192.

(39) Boruntea, C. R.; Lundegaard, L. F.; Corma, A.; Vennestrøm, P. N. R. Crystallization of AEI and AFX Zeolites through Zeolite-to-Zeolite Transformations. *Microporous Mesoporous Mater.* **2019**, *278*, 105–114.

(40) Muraoka, K.; Sada, Y.; Shimojima, A.; Chaikittisilp, W.; Okubo, T. Tracking the Rearrangement of Atomic Configurations during the Conversion of FAU Zeolite to CHA Zeolite. *Chem. Sci.* **2019**, *10*, 8533–8540.

(41) Chen, K.; Abdolrahmani, M.; Horstmeier, S.; Pham, T. N.; Nguyen, V. T.; Zeets, M.; Wang, B.; Crossley, S.; White, J. L. Brønsted–Brønsted Synergies between Framework and Noncrystalline Protons in Zeolite H-ZSM-5. *ACS Catal.* **2019**, *9*, 6124–6136.

(42) Deimund, M. A.; Harrison, L.; Lunn, J. D.; Liu, Y.; Malek, A.; Shayib, R.; Davis, M. E. Effect of Heteroatom Concentration in SSZ-13 on the Methanol-to-Olefins Reaction. *ACS Catal.* **2016**, *6*, 542–550.

(43) Ong, L. H.; Dömök, M.; Olindo, R.; Van Veen, A. C.; Lercher, J. A. Dealumination of HZSM-5 via Steam-Treatment. *Microporous Mesoporous Mater.* **2012**, *164*, 9–20.

(44) Wang, C.; Chu, Y.; Xu, J.; Wang, Q.; Qi, G.; Gao, P.; Zhou, X.; Deng, F. Extra-Framework Aluminum-Assisted Initial C−C Bond Formation in Methanol-to-Olefins Conversion on Zeolite H-ZSM-5. *Angew. Chemie - Int. Ed.* **2018**, *57*, 10197–10201.

(45) Dutta Chowdhury, A.; Yarulina, I.; Abou-Hamad, E.; Gurinov, A.; Gascon, J. Surface Enhanced Dynamic Nuclear Polarization Solid-State NMR Spectroscopy Sheds Light on Brønsted-Lewis Acid Synergy during the Zeolite Catalyzed Methanol-to-Hydrocarbon Process. *Chem. Sci.* **2019**, *10*, 8946–8954.

(46) Mota, C. J. A.; Bhering, D. L.; Rosenbach, N. A DFT Study of the Acidity of Ultrastable Y Zeolite: Where Is the Brønsted/Lewis Acid Synergism? *Angew. Chemie Int. Ed.* **2004**, *43*, 3050–3053.

(47) Zhang, J.; Shan, Y.; Zhang, L.; Du, J.; He, H.; Han, S.; Lei, C.; Wang, S.; Fan, W.; Feng, Z.; Liu, X.; Meng, X.; Xiao, F. Applied Catalysis B : Environmental Importance of Controllable Al Sites in CHA Framework by Crystallization Pathways for NH 3 -SCR Reaction. *Appl. Catal. B Environ.* **2020**, *277*, 119193.

(48) Nishitoba, T.; Yoshida, N.; Kondo, J. N.; Yokoi, T. Control of Al Distribution in the CHA-Type Aluminosilicate Zeolites and Its Impact on the Hydrothermal Stability and Catalytic Properties. *Ind. Eng. Chem. Res.* **2018**, *57*, 3914–3922.

(49) Liang, T.; Chen, J.; Qin, Z.; Li, J.; Wang, P.; Wang, S.; Wang, G.; Dong, M.; Fan, W.; Wang, J. Conversion of Methanol to Olefins over H-ZSM-5 Zeolite: Reaction Pathway Is Related to the Framework Aluminum Siting. *ACS Catal.* **2016**, *6*, 7311–7325.

(50) Janda, A.; Bell, A. T. Effects of Si/Al Ratio on the Distribution of Framework Al and on the Rates of Alkane Monomolecular Cracking and Dehydrogenation in H-MFI. *J. Am. Chem. Soc.* **2013**, *135*, 19193–19207.

(51) Wang, S.; Wang, P.; Qin, Z.; Chen, Y.; Dong, M.; Li, J.; Zhang, K.; Liu, P.; Wang, J.; Fan, W. Relation of Catalytic Performance to the Aluminum Siting of Acidic Zeolites in the Conversion of Methanol to Olefins, Viewed via a Comparison between ZSM-5 and ZSM-11. *ACS Catal.* **2018**, *8*, 5485–5505.

(52) Kim, S.; Park, G.; Woo, M. H.; Kwak, G.; Kim, S. K. Control of Hierarchical Structure and Framework-Al Distribution of ZSM - 5 via Adjusting Crystallization Temperature and Their E Ff Ects on Methanol Conversion. *ACS Catal.* **2019**, *9*, 2880–2892.

(53) Khalil, I.; Celis-Cornejo, C. M.; Thomas, K.; Bazin, P.; Travert, A.; Pérez-Martínez, D. J.; Baldovino-Medrano, V. G.; Paul, J. F.; Maugé, F. In Situ IR-ATR Study of the Interaction of Nitrogen Heteroaromatic Compounds with HY Zeolites: Experimental and Theoretical Approaches. *ChemCatChem* **2020**, *12*, 1095–1108.

(54) Khalil, I.; Jabraoui, H.; Lebègue, S.; Kim, W. J.; Aguilera, L. J.; Thomas, K.; Maugé, F.; Badawi, M. Biofuel Purification: Coupling Experimental and Theoretical Investigations for Efficient Separation of Phenol from Aromatics by Zeolites. *Chem. Eng. J.* **2020**, *402*, 126264.

(55) Gallas, J.; Goupil, J.; Vimont, A.; Lavalley, J.; Gil, B.; Gilson, J.; Miserque, O. Quantification of Water and Silanol Species on Various Silicas by Coupling IR Spectroscopy and In-Situ Thermogravimetry. *Langmuir* **2009**, *57*, 5825–5834.

(56) Emeis, C. A. Determination of Integrated Molar Extinction Coefficients for Infrared Absorption Bands of Pyridine Adsorbed on Solid Acid Catalysts. *J. Catal.* **1993**, *141*, 347–357.

(57) De Yoreo, J. J.; Gilbert, P. U. P. A.; Sommerdijk, N. A. J. M.; Penn, R. L.; Whitelam, S.; Joester, D.; Zhang, H.; Rimer, J. D.; Navrotsky, A.; Banfield, J. F.; Wallace, A. F.; Michel, F. M.; Meldrum, F. C.; Cölfen, H.; Dove, P. M. Crystallization by Particle Attachment in Synthetic, Biogenic, and Geologic Environments. *Science (80-.).* **2015**, *349*, 6247.

(58) Dai, H.; Shen, Y.; Yang, T.; Lee, C.; Fu, D.; Agarwal, A.; Le, T. T.; Tsapatsis, M.; Palmer, J. C.; Weckhuysen, B. M.; Dauenhauer, P. J.; Zou, X.; Rimer, J. D. Finned Zeolite Catalysts. *Nat. Mater.* **2020**, *19*, 1074–1080.

(59) Palčić, A.; Ordomsky, V. V.; Qin, Z.; Georgieva, V.; Valtchev, V. Tuning Zeolite Properties for a Highly Efficient Synthesis of Propylene from Methanol. *Chem. - A Eur. J.* **2018**, *24*, 13136–13149.

(60) Wu, Z.; Zhao, K.; Zhang, Y.; Pan, T.; Ge, S.; Ju, Y.; Li, T. Synthesis and Consequence of Aggregated Nanosized ZSM - 5 Zeolite Crystals for Methanol to Propylene Reaction. *Ind. Eng. Chem. Res.* **2019**, *58*, 10737–10749.

(61) Soulard, M.; Bilger, S.; Kessler, H.; Guth, J. L. Thermoanalytical Characterization of MFI-Type Zeolites Prepared Either in the Presence of OH- or of F- Ions. *Zeolites* **1987**, *7*, 463–470.

(62) Romannikov, V. N.; Mastikhin, V. M.; Hočevar, S.; Držaj, B. Laws Observed in the Synthesis of Zeolites Having the Structure of Zsm-5 and Varying Chemical Composition. *Zeolites* **1983**, *3*, 311–320.

(63) Scholle, K. F. M. G. J.; Veeman, W. S.; Frenken, P.; van der Velden, G. P. M. Characterization of Intermediate TPA-ZSM-5 Type Structures during Crystallization. *Appl. Catal.* **1985**, *17*, 233–259.

(64) Ikuno, T.; Chaikittisilp, W.; Liu, Z.; Iida, T.; Yanaba, Y.; Yoshikawa, T.; Kohara, S.; Wakihara, T.; Okubo, T. Structure-Directing Behaviors of Tetraethylammonium Cations toward Zeolite Beta Revealed by the Evolution of Aluminosilicate Species Formed during the Crystallization Process. *J. Am. Chem. Soc.* **2015**, *137*, 14533–14544.

(65) Chaikittisilp, W.; Yokoi, T.; Okubo, T. Crystallization Behavior of Zeolite Beta with Balanced Incorporation of Silicon and Aluminum Synthesized from Alkali Metal Cation-Free Mixture. *Microporous Mesoporous Mater.* **2008**, *116*, 188–195.

(66) Umeda, T.; Yamada, H.; Ohara, K.; Yoshida, K.; Sasaki, Y.; Takano, M.; Inagaki, S.; Kubota, Y.; Takewaki, T.; Okubo, T.; Wakihara, T. Comparative Study on the Different Interaction Pathways between Amorphous Aluminosilicate Species and Organic Structure-Directing Agents Yielding Different Zeolite Phases. *J. Phys. Chem. C* **2017**, *121*, 24324–24334.

(67) Ennaert, T.; Van Aelst, J.; Dijkmans, J.; De Clercq, R.; Schutyser, W.; Dusselier, M.; Verboekend, D.; Sels, B. F. Potential and Challenges of Zeolite Chemistry in the Catalytic Conversion of

Biomass. *Chem. Soc. Rev.* **2016**, *45*, 584–611.

(68) Zones, S. I. Conversion of Faujasites to High-Silica Chabazite SSZ-13 in the Presence of N,N,N-Trimethyl-1-Adamantammonium Iodide. *J. Chem. Soc. Faraday Trans.* **1991**, *87*, 3709–3716.

(69) Cundy, C. S.; Cox, P. A. The Hydrothermal Synthesis of Zeolites : Precursors , Intermediates and Reaction Mechanism. *Microporous Mesoporous Mater.* **2005**, *82*, 1–78.

(70) Crépeau, G.; Montouillout, V.; Vimont, A.; Mariey, L.; Cseri, T.; Maugé, F. Nature, Structure and Strength of the Acidic Sites of Amorphous Silica Alumina: An IR and NMR Study. *J. Phys. Chem. B* **2006**, *110*, 15172–15185.

(71) Khalil, I.; Thomas, K.; Jabraoui, H.; Bazin, P.; Maugé, F. Selective Elimination of Phenol from Hydrocarbons by Zeolites and Silica-Based Adsorbents—Impact of the Textural and Acidic Properties. *J. Hazard. Mater.* **2020**, *384*, 121397.

(72) Yashiki, A.; Honda, K.; Fujimoto, A.; Shibata, S.; Ide, Y.; Sadakane, M.; Sano, T. Hydrothermal Conversion of FAU Zeolite into LEV Zeolite in the Presence of Non-Calcined Seed Crystals. *J. Cryst. Growth* **2011**, *325*, 96–100.

(73) Lupulescu, A. I.; Rimer, J. D. In Situ Imaging of Silicalite-1 Surface Growth Reveals the Mechanism of Crystallization. *Science (80-.).* **2014**, *344*, 729–732.

(74) Kumar, M.; Choudhary, M. K.; Rimer, J. D. Transient Modes of Zeolite Surface Growth from 3D Gel-like Islands to 2D Single Layers. *Nat. Commun.* **2018**, *9*, 2129.

(75) Kumar, M.; Luo, H.; Román-Leshkov, Y.; Rimer, J. D. SSZ-13 Crystallization by Particle Attachment and Deterministic Pathways to Crystal Size Control. *J. Am. Chem. Soc.* **2015**, *137*, 13007−13017.

(76) Ni, Y.; Sun, A.; Wu, X.; Hai, G.; Hu, J.; Li, T.; Li, G. Facile Synthesis of Hierarchical Nanocrystalline ZSM-5 Zeolite under Mild Conditions and Its Catalytic Performance. *J. Colloid Interface Sci.* **2011**, *361*, 521–526.

(77) Wennmacher, J. T. C.; Li, T.; Zaubitzer, C.; Gemmi, M.; Mugnaioli, E.; Gruene, T.; van Bokhoven, J. A. Heterogeneity of Nano-Sized Zeolite Crystals. *Microporous Mesoporous Mater.* **2020**, *294*, 109897.

(78) Marcus, Y. A Simple Empirical Model Describing the Thermodynamics of Hydration of Ions of Widely Varying Charges, Sizes, and Shapes. *Biophys. Chem.* **1994**, *51*, 111–127.

(79) Baerlocher, C.; McCusker, L. B. Database of Zeolite Structures. Accessed on 2020 02 12.

(80) Blay, V.; Yokoi, T.; Peccatiello, K. A.; Clough, M.; Yilmaz, B. Engineering Zeolites for Catalytic Cracking to Light Olefins. *ACS Catal.* **2017**, *7*, 6542−6566.

(81) Palčić, A.; Valtchev, V. Analysis and Control of Acid Sites in Zeolites. *Appl. Catal. A Gen.* **2020**, *606*, 117795.

(82) Le, T. T.; Chawla, A.; Rimer, J. D. Impact of Acid Site Speciation and Spatial Gradients on Zeolite Catalysis. *J. Catal.* **2020**, *391*, 56–68.

(83) Verberckmoes, A. A.; Weckhuysen, B. M.; Schoonheydt, R. A. Spectroscopy and Coordination Chemistry of Cobalt in Molecular Sieves. *Microporous Mesoporous Mater.* **1998**, *22*, 165–178.

(84) Dědeček, J.; Kaucký, D.; Wichterlová, B. Co2+ Ion Siting in Pentasil-Containing Zeolites, Part 3.:

Co2+ Ion Sites and Their Occupation in ZSM-5: A VIS Diffuse Reflectance Spectroscopy Study. *Microporous Mesoporous Mater.* **2000**, *35–36*, 483–494.

(85) Hoser, H.; Krazyzanowski, S.; Trifiró, F. Optical Spectra of Co-Zeolites. *J. Chem. Soc. Faraday Trans. 1 Phys. Chem. Condens. Phases* **1975**, *71*, 665–669.

(86) Burton, A. W.; Zones, S. I. Studies in Surface Science and Catalysis, Elsevier, 2007, 137–179.

(87) De Ruiter, R.; Jansen, JC.; van Bekkum, H. On the Incorporation Mechanism of B and Al in MFI-Type Zeolite Frameworks. *Zeolites* **1992**, *12*, 56–62.

(88) Lewis, G. J.; Miller, M. A.; Moscoso, J. G.; Wilson, B. A.; Knight, L. M.; Wilson, S. T. Experimental Charge Density Approach To Zeolite Synthesis. *Stud. Surf. Sci. Catal.* **2004**, *154*, 364–372.

(89) Fedeyko, J. M.; Egolf-Fox, H.; Fickel, D. W.; Vlachos, D. G.; Lobo, R. F. Initial Stages of Self-Organization of Silica-Alumina Gels in Zeolite Synthesis. *Langmuir* **2007**, *23*, 4532–4540.

(90) Crea, F.; Nastro, A.; Nagy, J. B.; Aiello, R. Synthesis of Silicalite 1 from Systems with Different TPABr/SiO2 Ratios. *Zeolites* **1988**, *8*, 262–267.

(91) Mccormick, A. V.; Bell, A. T. The Solution Chemistry of Zeolite Precursors. *Catal. Rev.* **1989**, *31*, 97–127.

(92) Ren, N.; Subotić, B.; Bronić, J.; Tang, Y.; Dutour Sikirić, M.; Mišić, T.; Svetličić, V.; Bosnar, S.; Antonić Jelić, T. Unusual Pathway of Crystallization of Zeolite ZSM-5 in a Heterogeneous System: Phenomenology and Starting Considerations. *Chem. Mater.* **2012**, *24*, 1726–1737.

(93) Grey, C. P.; Vega, A. J. Determination of the Quadrupole Coupling Constant of the Invisible Aluminum Spins in Zeolite HY with 1H/27A1 TRAPDOR NMR. *J. Am. Chem. Soc.* **1995**, *117*, 8232–8242.

(94) Deng, F.; Yue, Y.; Ye, C. 1H/27Al TRAPDOR NMR Studies on Aluminum Species in Dealuminated Zeolites. *Solid State Nucl. Magn. Reson.* **1998**, *10*, 151–160.

(95) Engelhardt, G.; Michel, D. High-Resolution Solid-State NMR of Silicates and Zeolites. In *Applied Catalysis*; Wiley & Sons: New York, 1987.

(96) Anthony, J. L.; Davis, M. E. Assembly of Zeolites and Crystalline Molecular Sieves. In *Self-Organized Nanoscale Materials*; Springer, 2006; pp 159–185.

(97) Corma, A.; Davis, M. E. Issues in the Synthesis of Crystalline Molecular Sieves: Towards the Crystallization of Low Framework-Density Structures. *ChemPhysChem*. Wiley-VCH Verlag March 19, 2004, pp 304–313.

(98) Shin, J.; Ahn, N. H.; Camblor, M. A.; Cho, S. J.; Hong, S. B. Intraframework Migration of Tetrahedral Atoms in a Zeolite. *Angew. Chemie Int. Ed.* **2014**, *53*, 8949–8952.

(99) Gómez-Hortigüela, L.; Márquez-Álvarez, C.; Grande-Casas, M.; García, R.; Pérez-Pariente, J. Tailoring the Acid Strength of Microporous Silicoaluminophosphates through the Use of Mixtures of Templates: Control of the Silicon Incorporation Mechanism. *Microporous Mesoporous Mater.* **2009**, *121*, 129–137.

(100) Jansen, J. C.; Engelen, C. W. R.; van Bekkum, H. Zeolite Synthesis, American Chemical Society (ACS), 1989; 257–273.

(101) Li, T.; Krumeich, F.; Chen, M.; Ma, Z.; Bokhoven, J. A. Van. Defining Aluminum-Zoning during Synthesis of ZSM-5 Zeolites. **2020**, 734–739.

(102) Althoff, R.; Schulz-Dobrick, B.; Schüth, F.; Unger, K. Controlling the Spatial Distribution of Aluminum in ZSM-5 Crystals. *Microporous Mater.* **1993**, *1*, 207–218.

(103) Beyerlein, R. A.; Choi-Feng, C.; Hall, J. B.; Huggins, B. J.; Ray, G. J. Effect of Steaming on the Defect Structure and Acid Catalysis of Protonated Zeolites. *Top. Catal.* **1997**, *4*, 27–42.

(104) Holzinger, J.; Beato, P.; Lundegaard, L. F.; Skibsted, J. Distribution of Aluminum over the Tetrahedral Sites in ZSM-5 Zeolites and Their Evolution after Steam Treatment. *J. Phys. Chem. C* **2018**, *122*, 15595–15613.

(105) Ravi, M.; Sushkevich, V. L.; van Bokhoven, J. A. Towards a Better Understanding of Lewis Acidic Aluminium in Zeolites. *Nat. Mater.* **2020**, *19*, 1047–1056.

(106) Perea, D. E.; Arslan, I.; Liu, J.; Ristanović, Z.; Kovarik, L.; Arey, B. W.; Lercher, J. A.; Bare, S. R.; Weckhuysen, B. M. Determining the Location and Nearest Neighbours of Aluminium in Zeolites with Atom Probe Tomography. *Nat. Commun.* **2015**, *6*, 7589.

(107) Dusselier, M.; Deimund, M. A.; Schmidt, J. E.; Davis, M. E. Methanol-to-Olefins Catalysis with Hydrothermally Treated Zeolite SSZ-39. *ACS Catal.* **2015**, *5*, 6078–6085.

(108) Verboekend, D.; Chabaneix, A. M.; Thomas, K.; Gilson, J. P.; Pérez-Ramírez, J. Mesoporous ZSM-22 Zeolite Obtained by Desilication: Peculiarities Associated with Crystal Morphology and Aluminium Distribution. *CrystEngComm* **2011**, *13*, 3408–3416.

(109) Li, S.; Li, H.; Gounder, R.; Debellis, A.; Müller, I. B.; Prasad, S.; Moini, A.; Schneider, W. F. First-Principles Comparison of Proton and Divalent Copper Cation Exchange Energy Landscapes in SSZ-13 Zeolite. *J. Phys. Chem. C* **2018**, *122*, 23564–23573.